nature
cell biology

Alternate fast and slow stepping of a heterodimeric kinesin molecule

Kuniyoshi Kaseda[1,2], Hideo Higuchi[3] and Keiko Hirose[1,4]

A conventional kinesin molecule travels continuously along a microtubule in discrete 8-nm steps. This processive movement is generally explained by models in which the two identical heads of a kinesin move in a 'hand-over-hand' manner[1–4]. Here, we show that a single heterodimeric kinesin molecule (in which one of the two heads is mutated in a nucleotide-binding site) exhibits fast and slow (with the dwell time at least 10 times longer than that of the fast step) 8-nm steps alternately, presumably corresponding to the displacement by the wild-type and mutant heads, respectively. Our results provide the first direct evidence for models in which the roles of the two heads alternate every 8-nm step.

Various models have been proposed to explain the processive movement of a dimeric kinesin molecule. In the 'hand-over-hand' model[1–4], the two heads of a kinesin exchange their roles at every 8-nm step (Fig. 1a, left). In contrast, there are other models in which one of the heads is always leading; for example, the 'inchworm' model[5,6] (Fig. 1a, right). We thought that the most direct way to discriminate between these models would be to make a heterodimeric kinesin[7] in which the mechanochemical cycle rates of the two heads are different and to observe the time course of the displacement produced by a single heterodimer through optical trapping nanometry. For the hand-over-hand model, we expect the dwell time (time interval between successive 8-nm steps) of every other step to be different; for typical inchworm models, however, there should be no systematic changes in the dwell time (Fig. 1a).

To detect differences in the dwell time of every other step, if any, a heterodimeric kinesin in which the mechanochemical cycle rate of one head is at least several times slower than the other is required. In addition, the heterodimer should move processively and produce enough force. To make such a heterodimer, mutant kinesins with an altered nucleotide-binding motif were constructed[8]. When Arg 14 of a human conventional kinesin construct was mutated to alanine (R14A), the ATPase rate (1.5 ± 0.2 s^{-1} $head^{-1}$, mean ± standard deviation) and the microtubule-gliding speed (36 ± 5 nm s^{-1}) of the mutant homodimer were considerably slower than the wild type (27.6 ± 4.8 s^{-1} $head^{-1}$ and 636 ± 45 nm s^{-1}; Table 1). In optical trapping experiments, latex beads sparsely coated with the R14A/R14A homodimers bound briefly to the microtubule (association time ~200 ms; see Supplementary Information, Fig. S1) but did not show detectable movement at the single-molecule level (see Methods). At a

Table 1 ATPase measurements, micotubule-gliding assays and optical trapping experiments

Construct	ATPase assay		Gliding assay	Beads assay	
	ATPase rate (s^{-1} $head^{-1}$)	Km(MT) (μM)	Velocity (nm s^{-1})	Velocity (nm s^{-1})	Stall force (pN)
WT	27.6 ± 4.8	3.5 ± 2.0	636 ± 45	679 ± 156	5.4 ± 1.2
R14A/R14A	1.5 ± 0.2	0.1 ± 0.04	36 ± 15	58 ± 30*	n.d.*
WT/R14A	2.9 ± 0.7	1.7 ± 0.7	86 ± 30	85 ± 33	5.8 ± 1.3
	(2.8)		(68)	(106)	

All values are shown as the mean ± standard deviation. If a hand-over-hand model is assumed, k_{cat} and the velocity of the heterodimer is expected to be $k_h = 2/(1/k_w + 1/k_m)$ and $v_h = 2/(1/v_w + 1/v_m)$, respectively (k_w, v_w, k_m, v_m, k_{cat} and the velocities by the wild-type and mutant homodimers). The expected values (parentheses) are in good agreement with the experimental results. All measurements were performed in the presence of 1.5 mM ATP. *As R14A/R14A did not show processive behaviour at the single-molecule level, the velocity at a multiple-motor level is shown. The stall force of R14A/R14A could not be determined for the same reason.

[1]Gene Function Research Center, National Institute of Advanced Industrial Science and Technology (AIST), and [2]Japan Society for the Promotion of Science (JSPS), 1-1-1 Higashi, Tsukuba, Ibaraki 305-8562, Japan. [3]Department of Metallurgy, Graduate School of Engineering and Center for Interdisciplinary Research, Tohoku University, Sendai, Miyagi 980-8579, Japan. [4]Correspondence should be addressed to K.H. (e-mail: k.hirose@aist.go.jp)

Published online: 23 November 2003; DOI: 10.1038/ncb1067

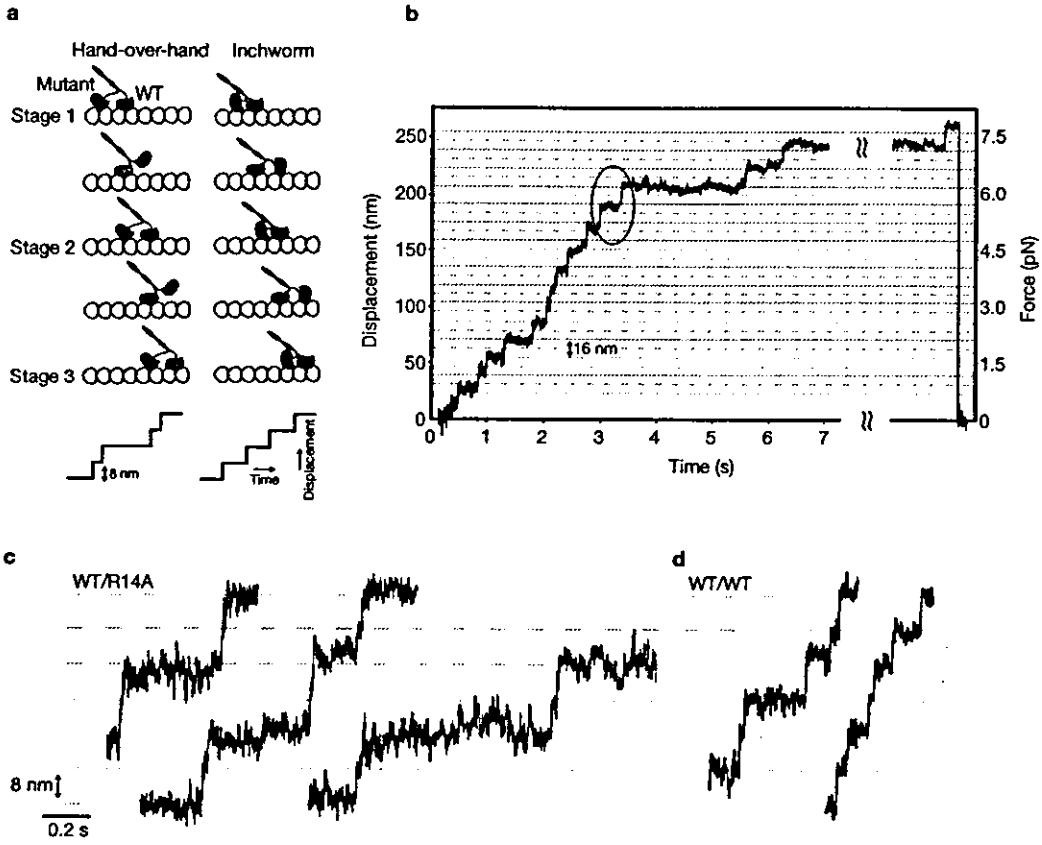

Figure 1 Time course of the displacement of a single heterodimeric kinesin molecule. **(a)** Two models explaining the processive movement of kinesin and expected changes in the dwell time when a heterodimer kinesin is used. According to the hand-over-hand model (left), two heads are interchanged at stage 2, compared with stage 1, but not in the inchworm model (right). Therefore, the dwell times at stages 1 and 2 are expected to be different only in the hand-over-hand model. Note that in practice, the dwell time fluctuates because the cycle includes stochastic processes. **(b)** A representative trace of the displacement of a bead coated with R14A/WT in an optical trap. In most of the cases, the steps seem to be 16 nm (horizontal solid gridlines). **(c)** An enlarged view of the traces in **b**. These traces reveal a shoulder at ~8 nm (dotted lines), indicating that the observed 16-nm step consists of two successive 8-nm steps. The far-left trace is an enlarged view of the area circled in **b**. **(d)** Control experiments using the wild-type homodimers show clear 8-nm steps.

higher homodimer concentration, where ~60% of the beads showed attachment signals, ~10% of the beads moved continuously (see Supplementary Information, Fig. S2), indicating that R14A/R14A-coated beads can move along a microtubule when more than one molecule interacts with the microtubule. Michaelis-Menten fitting of the velocities at varying ATP concentrations showed that R14A/R14A has a markedly decreased affinity for ATP when compared with wild type (K_m(ATP) of ~5 mM and ~30 μM for R14A/R14A and WT/WT, respectively; see Supplementary Information, Fig. S3). In the presence of 1.5 mM ATP, the velocity of R14A/R14A was 58 ± 30 nm s^{-1}, less than 10% of the wild-type homodimer rate (679 ± 156 nm s^{-1}).

As the velocity of the R14A mutant is slow enough when compared with the wild type, we made the heterodimeric kinesin, WT/R14A. In contrast to R14A/R14A, beads coated with WT/R14A moved slowly but continuously at the single-molecule level (Fig.1b). The velocity of WT/R14A, calculated from the initial slope of the displacement traces, was 85 ± 33 nm s^{-1}, which is 12.5% that of the wild-type homodimer. Microtubule-gliding assays gave similar results (Table 1). The averaged maximum force was as high as wild type (5.8 ± 1.3 pN and 5.4 ± 1.2 pN for WT/R14A and WT/WT, respectively). However, although the wild-type homodimer clearly showed 8-nm steps (Fig. 1d), the step size of WT/R14A seemed to be 16 nm (Fig.1b). Closer inspection of each 16-nm step revealed a shoulder at approximately 8 nm (Fig. 1c). The averaged height of the shoulder (ΔX1 in Fig. 2a) was 8.2 ± 1.5 nm (mean ± standard deviation), and the size of the step after the shoulder (ΔX2) was 7.8 ± 1.4 nm. These two step sizes are statistically indistinguishable ($P = 0.05$). The results described here indicate that the observed 16-nm step is actually two successive 8-nm steps; the second 8-nm (ΔX2) step occurred after a very short dwell time.

The above results suggest that for the WT/R14A heterodimer, a step followed by a short dwell time (here, we call it a fast step) may alternate with one followed by a long dwell time (slow step). Fig. 2b shows examples of how the dwell time of successive steps changed. In contrast to WT/WT, which showed no systematic changes in dwell time, WT/R14A took a step with a long dwell time (typically >60 ms) and one with a short dwell time (typically <30 ms) alternately in most instances (>94%), irrespective of the applied load. We also compared the distributions of the dwell times of steps that occurred directly after a short dwell time (<20 ms; Fig. 2c, red) with those after a long dwell time (>100 ms; Fig. 2c, blue). The majority of steps after a short dwell time had a dwell time longer than 60 ms, whereas most of the

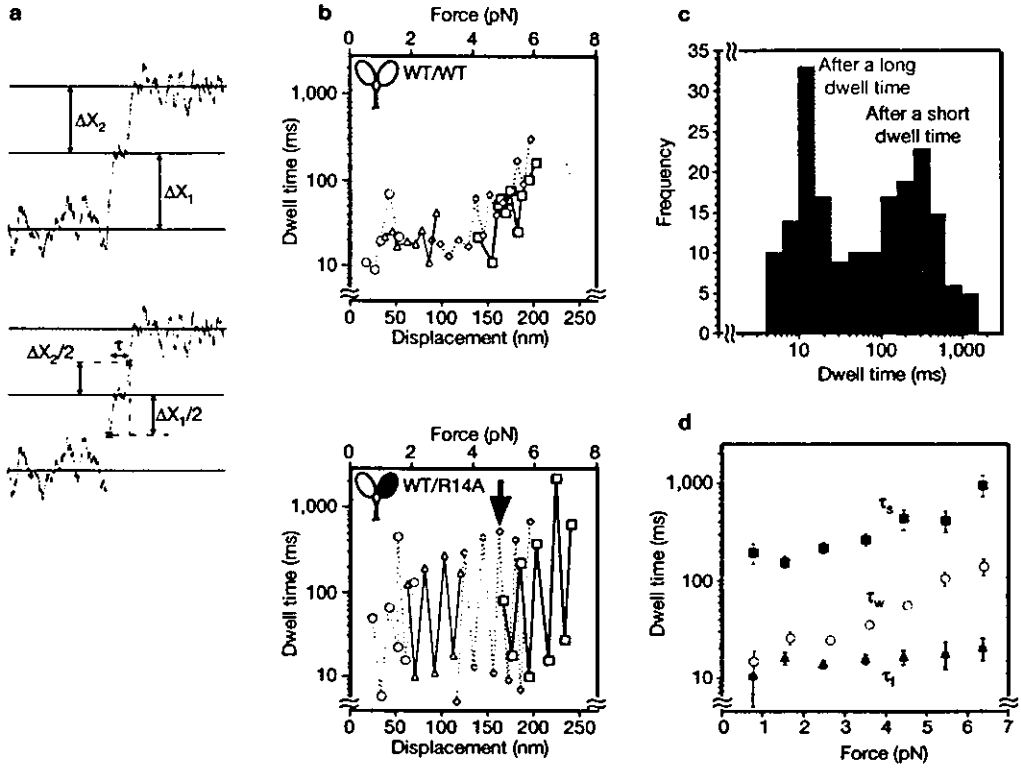

Figure 2 Dwell time analysis. (a) A displacement trace showing how step sizes (ΔX1, ΔX2) and dwell time (τ) were measured. (b) The dwell time of successive steps recorded for several beads and plotted logarithmically against bead displacement. The corresponding force is also shown on the upper axis. WT/R14A, but not WT/WT, showed long and short dwell times, alternately. (c) Distribution of the dwell time of the step directly after a step with a long (>100 ms) dwell time (blue), and those following a step with a short (<20 ms) dwell time (red). (d) Force dependency of the averaged dwell time (mean ± s.e.m.). Dwell times increased with load. The dwell time of the slow step (τs; blue square) of WT/R14A was at least 10 times longer than that of the fast step (τf; black triangle) at all force levels. τf was clearly shorter than the dwell time of WT/WT (τw; red circle) at a high load.

steps after a long dwell time had a dwell time shorter than 30 ms. These results can only be explained by models in which the roles of the two heads alternate every 8 nm.

The ATPase rate ($2.9 \pm 0.7\ s^{-1}$ head^{-1}) and the velocity (86 ± 30 nm s^{-1} in microtubule-gliding assays and 85 ± 33 nm s^{-1} in beads assays) of WT/R14A were also consistent with models in which the two heads work alternately (see Table 1 legend). This is different from our previous heterodimers with microtubule-binding defects, which showed a simple average of the ATPase rates from wild-type and mutant homodimers[7]. These results indicate that WT/R14A, unlike our previous weak-binding heterodimers, retains the tight coupling mechanism.

The simplest interpretation for the above observations is that the fast steps are caused by the wild-type head and the slow steps are caused by the mutant head. The force dependency of the averaged dwell times (see Methods) of the fast steps (τf), the slow steps (τs) and those of the wild-type homodimer (τw) are shown in Fig. 2d. At all force levels, τs was significantly longer than τw. We could not measure the dwell time of the R14A/R14A homodimer, because it did not move processively. The maximum velocity of R14A/R14A at a multiple motor level (58 nm s^{-1}) gives a rate of ~140 ms per 8-nm step at a low load. In addition, the association time of the R14A/R14A homodimer was ~200 ms (see Supplementary Information, Fig. S1). These rates are similar to τs at a low load (150–200 ms at 1–2 pN), in agreement with the idea that the R14A mutant head of a heterodimer is responsible for the slow step. At a low load (1–3 pN), the dwell time of the fast step (τf) was similar to τw, supporting the idea that the wild-type head of WT/R14A is responsible for the fast step. However, τf showed lower load dependency than the wild type. At a higher load (>4 pN), τf was significantly shorter than τw.

We wondered how the fast step of a heterodimer could be even faster than the steps of the wild-type kinesin. With the wild type kinesins, previous biochemical studies indicated that ATP binding or hydrolysis by one of the heads triggers binding of the second head to tubulin[3,9,10], followed by ATP binding/hydrolysis by the second head. However, as R14A is mutated in the site that is thought to interact with the adenine ring, the ATP-binding rate of the R14A head is likely to be slower than that of the wild type. In fact, K_m(ATP), determined from the velocity of R14A/R14A at a multiple molecular level, was >100 times higher than that of the wild-type molecule (see above). Thus, it is possible that the wild-type head in WT/R14A can bind and/or hydrolyse a new ATP molecule during the long waiting time, before the R14A head does so. Once the mutant head is ready and the slow step is complete, the already active, wild-type head could produce the next step quickly, resulting in a step with a shorter dwell time[11]. The probability of the wild-type head entering the active state during the waiting time should be greater at a high load, because τs becomes longer. This could explain why τf was significantly shorter than τw at a high load, but more similar to τw when the force was small.

Recently published work using single-molecule fluorescence polarization[12,13] demonstrated that the fluorescently labelled light-chain region of one of the heads of myosin V shows two different, well-defined angles

and two different sizes of displacement alternately, also supporting a hand-over-hand mechanism. Thus, alternate stepping might be a common mechanism for the dimeric protein motors to move processively. In the present study, we used optical trapping nanometry techniques to visualize elementary processes of an actively translocating heterodimeric kinesin molecule. A single heterodimeric kinesin showed a step with a long dwell time alternating with one with a short dwell time. Our results provide the first direct evidence for a model in which the roles of the two heads of a kinesin molecule alternate as it displaces by 8 nm, such as the hand-over-hand model. □

METHODS

Expression constructs and protein purification. The procedures for obtaining mutant homodimeric and heterodimeric kinesins have been described in detail previously[7]. To make the R14A mutant, Arg 14 of K432 (amino acids 1–432 of the human kinesin) was mutated to alanine using the QuickChange mutagenesis kit (Stratagene, West Cedar Creek, TX). The R14A/R14A homodimer was prepared with an amino-terminal glutathione *S*-transferase (GST) tag and an additional carboxy-terminal sequence to be biotinylated. The expressed proteins were purified with a glutathione 4B–Sepharose resin (Amersham Pharmacia, Tokyo, Japan). To construct the WT/R14A heterodimer, a DNA fragment encoding the wild-type kinesin with a C-terminal His tag and a fragment encoding the R14A mutant kinesin with an N-terminal GST tag and a C-terminal biotinylation sequence were placed side by side in a vector. The WT/R14A heterodimer was purified first with a glutathione resin to separate WT/WT, and then with a Ni-NTA–Agarose resin (Qiagen, Tokyo, Japan) to separate R14A/R14A. GST was removed by thrombin treatment (Sigma, St Louis, MO).

Optical trapping nanometry. The apparatus for the trapping nanometry experiments was as described previously[14]. Streptavidin-coated 0.2-μm beads were incubated with biotinylated kinesins, prepared as described above, and introduced into an assay chamber. The kinesin concentration (<75 nM) was determined so that the probability of kinesin-coated beads moving on a microtubule was 0.15–0.30. Under this condition, it is considered that only a single kinesin molecule is statistically involved in the movement of a bead[15,16]. Beads were optically trapped and positioned near a microtubule bound directly onto a coverslip. The bead positions were recorded at a sampling rate of 10 kHz using MacLab software[11,14,17] (AD Instruments, New South Wales, Australia). Experiments were performed in 80 mM Pipes at pH 6.8, 2 mM $MgCl_2$, 100mM NaCl, 1 mM EGTA and 1.5 mM ATP in the presence of an oxygen scavenging system at 24–26 °C. The trap stiffness (0.03 pN nm^{-1}) was calibrated from the amplitude of thermal diffusion[11,18].

Analysis of step size and dwell time. Displacement traces were low-pass-filtered at 200 Hz. Step sizes (ΔX1 and ΔX2 in Fig. 2a) were determined as the difference between the plateau levels in the traces. For a short step, it was difficult to measure the dwell time from the duration of the plateau. Therefore, the dwell time was defined as shown in Fig. 2a. From these measured dwell times, we classified the individual steps of the heterodimers into fast and slow steps. However, because of the fluctuation and force-dependency of the dwell time, we could not classify them simply by the length of the dwell time. Therefore, we plotted the dwell time of successive steps as in Fig. 2a and chose only those points that could be definitively considered as fast or slow steps. For example, the point indicated by an arrow in Fig. 2b has a dwell time of ~500 ms and is sandwiched between steps with much shorter dwell times (<20 ms). We categorized this kind of a step as slow and then defined the steps directly before or after it as fast. The second steps were considered to be slow steps. Occasionally, two successive steps had a dwell time shorter than 20 ms (or longer than 80 ms) followed by a long (or short) step. We ignored these small percentages of steps (~2% for each). Within each population classified as above, the dwell time/force data sets from different traces were grouped according to the force. At every 1.0 pN, the dwell time and force were averaged within the group. The averaged dwell time was plotted against the corresponding averaged force (Fig. 2d). For the wild type, the dwell time/force data were similarly analysed but were not classified into fast and slow steps.

Note: Supplementary Information is available on the Nature Cell Biology website.

ACKNOWLEDGEMENTS

We thank L. Amos for comments on the manuscript. This work was aided by support from the Human Frontier Science Program (H.H. and K.H.) and the Japan Society for the Promotion of Science (K.K.).

COMPETING FINANCIAL INTERESTS

The authors declare that they have no competing financial interests.

Received 25 July 2003; accepted 20 October 2003
Published online at http://www.nature.com/naturecellbiology.

1. Howard, J. The mechanics of force generation by kinesin. *Biophys J.* **68**, S245–S253; S253–S255 (1995).
2. Block, S. M., Goldstein, L. S. & Schnapp, B. J. Bead movement by single kinesin molecules studied with optical tweezers. *Nature* **348**, 348–352 (1990).
3. Hackney, D. D. Evidence for alternating head catalysis by kinesin during microtubule-stimulated ATP hydrolysis. *Proc. Natl Acad. Sci. USA* **91**, 6865–6869 (1994).
4. Vale, R. D. & Milligan, R. A. The way things move: looking under the hood of molecular motor proteins. *Science* **288**, 88–95 (2000).
5. Block, S. M. & Svoboda, K. Analysis of high resolution recordings of motor movement. *Biophys J.* **68**, S2305–S2415 (1995).
6. Hua, W., Chung, J. & Gelles, J. Distinguishing inchworm and hand-over-hand processive kinesin movement by neck rotation measurements. *Science* **295**, 844–848 (2002).
7. Kaseda, K., Higuchi, H. & Hirose, K. Coordination of kinesin's two heads studied with mutant heterodimers. *Proc. Natl Acad. Sci. USA* **99**, 16058–16063 (2002).
8. Vale, R. D. Switches, latches, and amplifiers: common themes of G proteins and molecular motors. *J. Cell Biol.* **135**, 291–302 (1996).
9. Cross, R. A. *et al.* The conformational cycle of kinesin. *Phil. Trans R Soc. Lond B* **355**, 459–464 (2000).
10. Ma, Y. Z. & Taylor, E. W. Interacting head mechanism of microtubule-kinesin ATPase. *J. Biol. Chem.* **272**, 724–730 (1997).
11. Kojima, H., Muto, E., Higuchi, H. & Yanagida, T. Mechanics of single kinesin molecules measured by optical trapping nanometry. *Biophys J.* **73**, 2012–2022 (1997).
12. Forkey, J. N., Quinlan, M. E., Shaw, M. A., Corrie, J. E. & Goldman, Y. E. Three-dimensional structural dynamics of myosin V by single-molecule fluorescence polarization. *Nature* **422**, 399–404 (2003).
13. Yildiz, A. *et al.* Myosin V walks hand-over-hand: single fluorophore imaging with 1.5-nm localization. *Science* **300**, 2061–2065 (2003).
14. Nishiyama, M., Muto, E., Inoue, Y., Yanagida, T. & Higuchi, H. Substeps within the 8-nm step of the ATPase cycle of single kinesin molecules. *Nature Cell Biol.* **3**, 425–428 (2001).
15. Svoboda, K., Schmidt, C. F., Schnapp, B. J. & Block, S. M. Direct observation of kinesin stepping by optical trapping interferometry. *Nature* **365**, 721–727 (1993).
16. Svoboda, K. & Block, S. M. Force and velocity measured for single kinesin molecules. Force and velocity measured for single kinesin molecules. *Cell* **77**, 773–784 (1994).
17. Higuchi, H., Muto, E., Inoue, Y. & Yanagida, T. Kinetics of force generation by single kinesin molecules activated by laser photolysis of caged ATP. *Proc. Natl Acad. Sci. USA* **94**, 4395–4400 (1997).
18. Visscher, K. & Block, S. M. Versatile optical traps with feedback control. *Methods Enzymol.* **298**, 460–489 (1998).

International weekly journal of science

nature

Processivity of the single-headed kinesin KIF1A through biased binding to tubulin

Yasushi Okada[*1], Hideo Higuchi[*2] & Nobutaka Hirokawa[*1]

[*1]*Department of Cell Biology and Anatomy, University of Tokyo, Graduate School of Medicine, Hongo, Bunkyo-ku, Tokyo 113-0033, Japan*
[*2]*Department of Metallurgy, Graduate School of Engineering, and Center for Interdisciplinary Research, Tohoku University, Sendai 980-8579, Japan*

Reprinted from Nature, Vol. 424, No. 6948, pp. 574–577, 31 July 2003

Processivity of the single-headed kinesin KIF1A through biased binding to tubulin

Yasushi Okada[1], Hideo Higuchi[2] & Nobutaka Hirokawa[1]

[1]*Department of Cell Biology and Anatomy, University of Tokyo, Graduate School of Medicine, Hongo, Bunkyo-ku, Tokyo 113-0033, Japan*
[2]*Department of Metallurgy, Graduate School of Engineering, and Center for Interdisciplinary Research, Tohoku University, Sendai 980-8579, Japan*

Conventional isoforms of the motor protein kinesin behave functionally not as 'single molecules' but as 'two molecules' paired. This dimeric structure poses a barrier to solving its mechanism[1–4]. To overcome this problem, we used an unconventional kinesin KIF1A (refs 5, 6) as a model molecule. KIF1A moves processively as an independent monomer[7,8], and can also work synergistically as a functional dimer[9]. Here we show, by measuring its movement with an optical trapping system[10], that a single ATP hydrolysis triggers a single stepping movement of a single KIF1A monomer. The step size is distributed stochastically around multiples of 8 nm with a gaussian-like envelope and a standard deviation of 15 nm. On average, the step is directional to the microtubule's plus-end against a load force of up to 0.15 pN. As the source for this directional movement, we show that KIF1A moves to the microtubule's plus-end by ~3 nm on average on binding to the microtubule, presumably by preferential binding to tubulin on the plus-end side. We propose a simple physical formulation to explain the movement of KIF1A.

As the tag for the manipulation and measurement, we attached a 0.2-μm bead to one end of the wild-type KIF1A construct A382, residues 1–382 of mouse KIF1A (not containing the neck of conventional kinesin[7,8]; Supplementary Information 1). The rapid response time (0.25 ms)[10] and the small pivotal and the rotational brownian movement of the 0.2-μm bead enabled us to detect clearly the small and fast movement at low load[11]. For most assays, biotinylated A382 was attached to the streptavidin-coated bead. For some assays, non-biotinylated A382 was attached to the bead via the Fab fragment of an anti-His-tag antibody to avoid the possibility of pseudo-dimerization on streptavidin. Furthermore, to examine the contribution by the structural change at the carboxy-terminal neck linker[12], the bead was attached to the amino terminus or the C terminus of A382 (Fig. 1a).

When in contact with a microtubule on a coverglass, the KIF1A bead showed stochastic oscillation (Fig. 1b). The movement was not affected by the immobilization method of KIF1A or by its anchoring position on the bead. The Poisson statistics analysis of the fraction of the moving beads as a function of the mixing ratio of KIF1A to beads[13,14] confirmed that a single KIF1A molecule was sufficient for the movement (Supplementary Information 2). For the experiments below, we used a mixing ratio at which the fraction of the bead movement was less than 0.3, so that more than 99% of the moving beads would be driven by only one molecule[10]. At 10-fold higher mixing ratios, some of the beads showed qualitatively different movement (Supplementary Information 2), similar to the movement by artificially dimerized KIF1A (ref. 9). The lack of this type of movement confirmed that we were actually analysing single-motor events.

The stochastic oscillation of the KIF1A bead cannot be explained by simple brownian movement interrupted by binding events, because the oscillation shifted to the microtubule plus-end, far exceeding the range of thermal fluctuation (Fig. 1b; Supplementary Information 3). Furthermore, the same KIF1A bead moved processively to the microtubule plus-end for more than 1 μm when the optical trap was turned off (Fig. 1c). This indicates that the oscillation reflects the active tug-of-war between the movement of KIF1A and the external load by the fixed-beam optical trap. With conventional kinesin, this tug-of-war results in a stall, because it rarely moves backwards[11]. In contrast, KIF1A sometimes moves backwards even under no load[7,8]. External load would affect the probability of forward movement, leading to stochastic oscillation. Consistently, the mean velocities at various force levels were linearly related to the force (Fig. 1d).

When ATPase turnover was slowed by decreasing the ATP concentration, the KIF1A bead showed a clear bidirectional stepwise movement (Fig. 2a, b). The interval between steps (dwell time) and the duration of the stepping movement (stepping time) followed single-exponential distributions (Fig. 2c, d). The mean of the dwell time was equal to the duration of the nucleotide-free state of a single ATPase cycle (Fig. 2e), indicating that a single ATP hydrolysis produces a single mechanical step (Supplementary Information

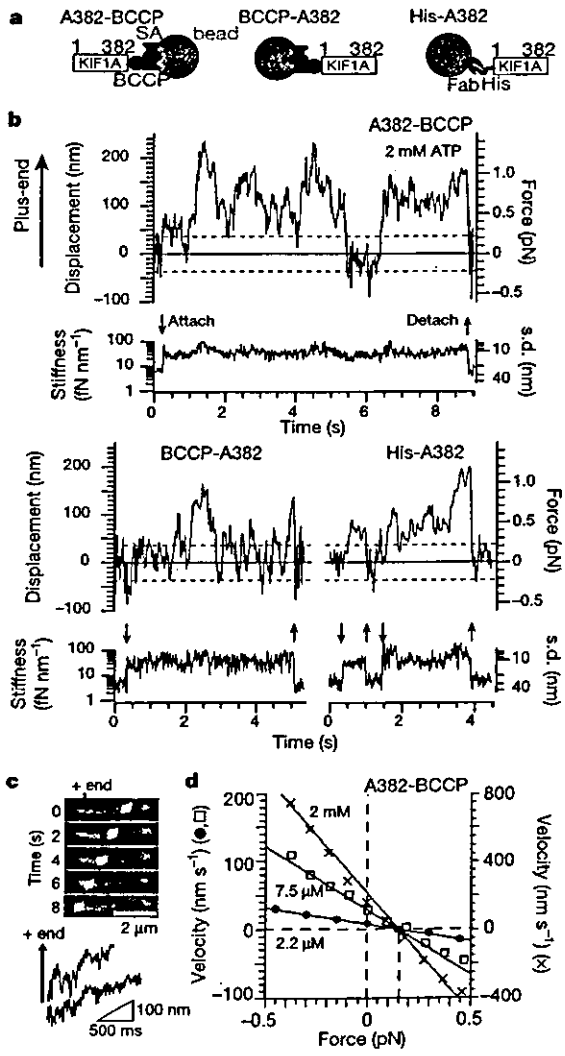

Figure 1 Movement of KIF1A beads. **a**, Design of the bead. BCCP, biotinylation tag; SA, streptavidin; Fab, Fab fragment of anti-His-tag antibody (His). (See Supplementary Information 1 for details.) **b**, Displacement of KIF1A beads. Red lines show the range of the thermal fluctuation (s.d.) of the free bead. Traces of stiffness indicate the attachment and detachment of the KIF1A to and from the microtubule. **c**, Processive movement of the KIF1A bead after the optical trap has been turned off. **d**, Force–velocity relationship. The lines show the predictions from the model in Fig. 3c and Supplementary Information 5. Crosses, 2 mM ATP; squares, 7.5 μM ATP; circles, 2.2 μM ATP.

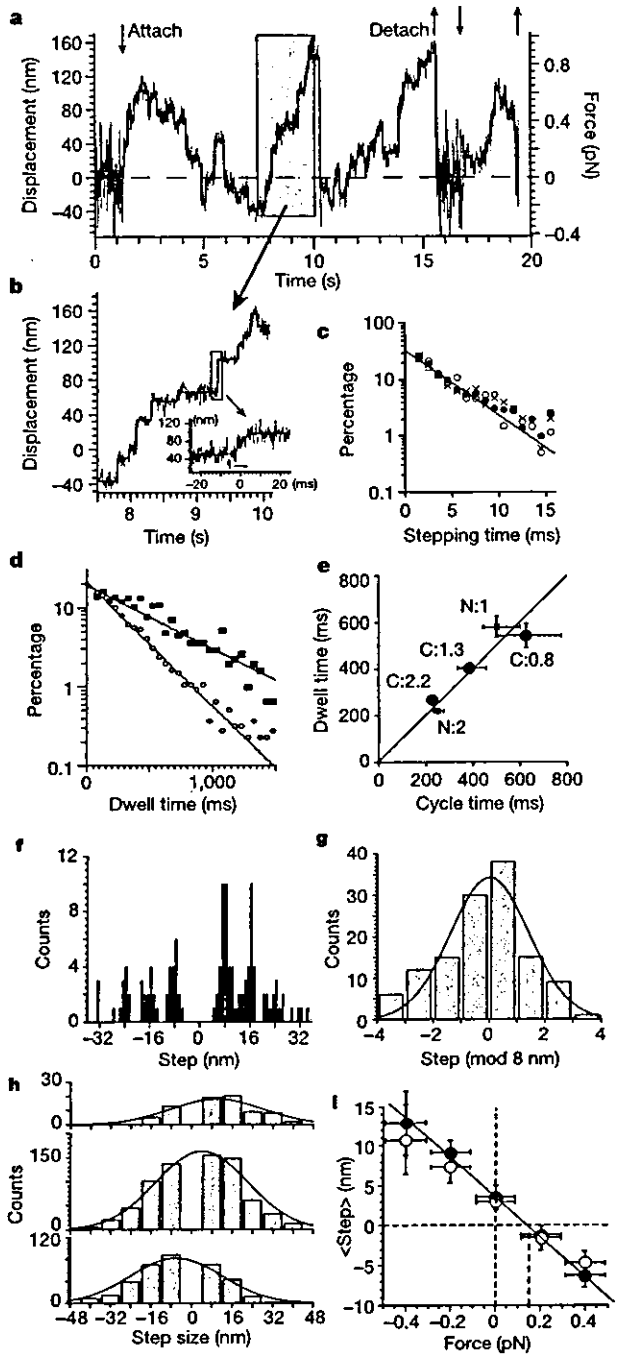

Figure 2 Stepping movement of KIF1A beads. **a**, Raw (grey) and filtered (black) displacement (A382-BCCP; [ATP] = 2.2 μM). **b**, Higher temporal resolution view of **a**. **c**, ATP-independent (squares, 0.8 μM; crosses, 1.3 μM; circles, 2.2 μM) distribution of the stepping time. **d**, ATP-dependent (squares, 0.8 μM; circles, 2.2 μM) distribution of the dwell time. In **d**, squares, 0.8 μM ATP; circles, 2.2 μM ATP. **e**, Comparison of the dwell time (**d**) with the ATPase cycle time (Supplementary Information 1). The construct (N, BCCP-A382; C, A382-BCCP) and the ATP concentration in μM are indicated next to the data points. **f**, Distribution of the step size (A382-BCCP). **g**, Deviation of the step size around multiples of 8 nm. The data in **f** are re-plotted with the best-fit gaussian curve (mean 0, s.d. 3 nm). **h**, Load dependence of the distribution of the step size (A382-BCCP, 2.2 μM ATP). Steps of at least ±8 nm were scored for their size and the force level, and plotted with the best-fit gaussian curves (see Methods). A positive load means that the bead is pulled towards the microtubule minus end. Top panel, −0.5 to −0.3 pN; middle panel, −0.1 to 0.1 pN; bottom panel, 0.3 to 0.5 pN. **i**, Linear dependence of the mean step on load, at 2 μM ATP. The line shows the theoretical prediction on the basis of $\langle s \rangle = \delta - (D\tau/k_BT)F$. Filled circles, A382-BCCP; open circles, BCCP-A382. (See the inset to Supplementary Information 5 for details.)

3). The size and the direction of this step varied stochastically (Fig. 2f), a behaviour very different from the regular 8-nm step of a conventional kinesin dimer[11,15]. However, the step size was distributed around multiples of 8 nm (Fig. 2f, g), reflecting the periodicity of the binding site on the microtubule[12,16]. The envelope of this discrete distribution was approximately gaussian. Its standard deviation (15 ± 2 nm) was insensitive to load, whereas its mean showed a linear dependence on load (Fig. 2h, i).

This gaussian-type envelope of the distribution of the step size indicates that the stepping movement contains one or more diffusion-like processes, which agrees with our previous result[7]. However, diffusion alone cannot produce a directional movement. Directional movement should occur either immediately before diffusion (Fig. 3c, step 2) or immediately after diffusion (Fig. 3c, step 4). To examine these possibilities, we measured the movement at the transition from the ADP-bound diffusion state into the rigor-binding state by using the experimental framework established to detect the movement of myosin when it binds to actin[17]. The position of the KIF1A bead was measured before and after its binding to the microtubule (Fig. 3a). To confirm that KIF1A bound correctly to the microtubule, ATP was added to the buffer (2 μM) and only the binding events followed by the stepping movement were scored. In this condition, free KIF1A remains in the ADP-bound state owing to the very slow release of ADP (less than 0.003 s^{-1}). Then KIF1A releases ADP and binds to one of the binding sites. From the transient kinetic measurements of other kinesins[4,18], this transition state is expected to have the same properties as the intermediate state during processive movement. The position before and after the binding to the microtubule was measured by averaging out the pivotal brownian movement of the bead.

The ensemble average of ~2,000 binding events (Fig. 3b) showed a rapid plus-end-directed displacement after binding, followed by a slow plus-end-directed movement. The latter slow movement agreed with the mean velocity of the KIF1A movement, reflecting the ensemble average of KIF1A's stepping motion by ATP hydrolysis (Fig. 3a, blue arrow). The size of the rapid displacement was estimated by extrapolating the slope of the slow movement to zero time as 2.8 ± 0.8 nm. This burst-type displacement is coupled with the release of ADP or the binding of KIF1A to the microtubule before ATP binding, because ATP binding takes ~250 ms on average at 2 μM ATP. The simplest interpretations of the rapid displacement are that KIF1A preferentially selects the binding site on the plus-end side or changes the structure by ADP release as proposed by ATP binding[3,12].

On the basis of these results, we can quantitatively model the stepping movement of KIF1A (Fig. 3c, Supplementary Information 5). The hydrolysis of newly bound ATP into ADP releases KIF1A from the binding site on the microtubule (Fig. 3c, step 2). Let the (putative) directional movement of the KIF1A bead during this process be $\delta_{release}$ (in nm). This parameter has not yet been measured, but contains the displacement by the power stroke and other putative mechanical processes. The ADP-bound form of KIF1A moves along the microtubule by one-dimensional diffusion (step 3) with diffusion coefficient D (26 ± 6 $nm^2 ms^{-1}$; Supplementary Information 1). The theory of brownian movement holds that the mean and variance of the displacement under load force F are given by $-(\tau D/k_BT)F$ and $2D\tau$, respectively (Supplementary Information 5), where k_B, T and τ denote the Boltzman constant, the temperature (299 ± 1 K) and the duration of this diffusive movement (4 ± 1 ms, measured as the stepping time in Fig. 2c), respectively. Finally, KIF1A binds again to the microtubule and ADP is released (Fig. 3c, step 4). KIF1A moves to the plus-end by δ_{bind} (2.8 ± 0.8 nm) on average (Fig. 3b). The step movement is the sum of these factors, and its mean and standard deviation are calculated to be

$$\langle s \rangle = \delta_{release} + \delta_{bind} - (D/k_BT)\tau F = \delta_{release} + 2.8 - 25F \text{ (in nm)}$$

and

$$\sigma(s) = (2D\tau)^{1/2} = 14 \text{ (in nm)}$$

respectively. These theoretical estimates fit the observations quantitatively (Fig. 2h, i), and the value for $\delta_{release}$ is estimated to be 0.8 ± 1 nm (Fig. 2i). The same theoretical results also explain the linear force–velocity relationship (Fig. 1d). The velocity of the movement V is expressed as $V = \langle s \rangle k_{cat} = (3.6 - 25F)k_{cat}$. Under the assumption that the load force does not significantly affect the turnover rate of ATP hydrolysis, k_{cat}, in this weak load range, this equation gives a linear force–velocity relationship (Supplementary Information 5). This equation with the k_{cat} values for A382 (Supplementary Information 1) agrees well with observation (Fig. 1d).

The nearly zero value for the estimate of $\delta_{release}$ implies that the power stroke or the putative movement during the period from the ATP binding to its hydrolysis into ADP does not contribute much to the net movement. This is consistent with our failure to detect a difference in the step size between N-terminally and C-terminally anchored beads (Fig. 2i), because the power stroke of the C-terminal neck would be reflected in a difference in the movement between beads anchored at the different termini. This also implies that the movement of KIF1A can be modelled simply by the theory of a flush-ratchet-type brownian motor[19,20]. In this model, δ_{bind} reflects the bias in selection of the binding site. This bias might have been introduced by the artificial linkage of the motor to the bead. However, a free KIF1A motor moves processively, like the motor attached to the bead (Supplementary Information 1). Thus, the effect of anchoring to the bead is negligible and the bias reflects the asymmetry in the binding potential between KIF1A and the microtubule[7,8].

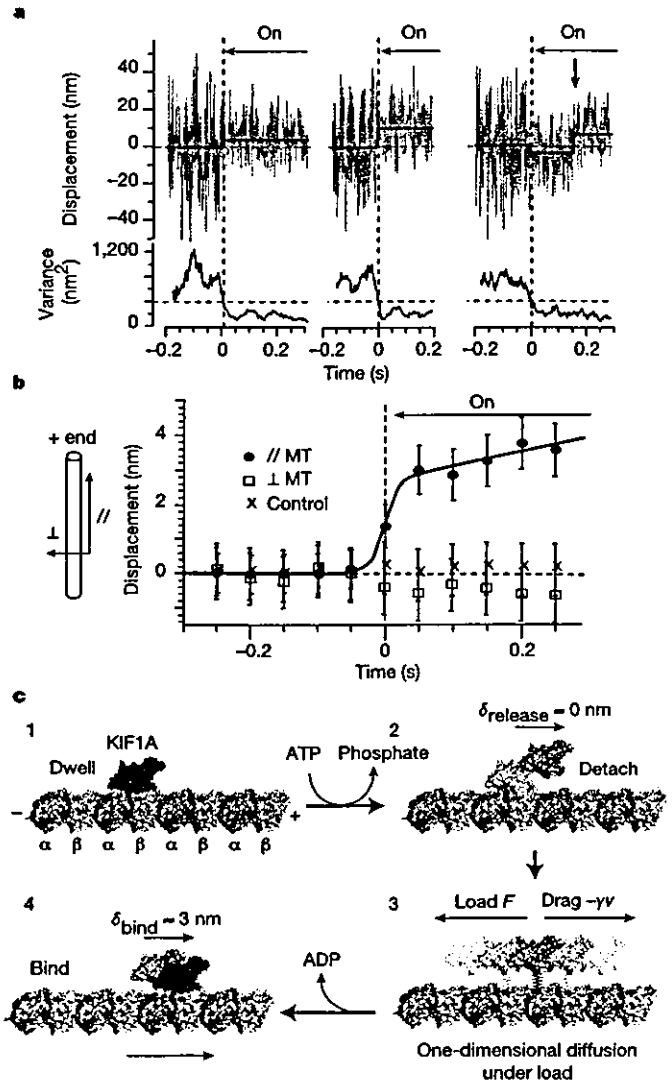

Figure 3 Plus-end-directed movement after binding to the microtubule. **a**, Raw (grey) and filtered (black) displacement with variance (red). The blue arrow shows the stepping by the ATPase reaction. **b**, Ensemble mean ± s.e.m. of the KIF1A bead displacement (red) after binding to the microtubule. To minimize possible artefacts in the shift, about half of the measurement ($n = 875$) was with plus-end-up microtubules (on the monitor) and the rest ($n = 774$) was with plus-end-down microtubules. Means of the bead position 50 ms after binding to the plus-end-up and plus-end-down microtubules were 3.2 and 3.1 nm, respectively, indicating no artefact in the shift. As controls for the null net displacement, the off-axis displacement (green, $n = 1649$) and the displacement after non-specific binding to the coverglass (blue, $n = 1420$) are also indicated. (See Methods for details.) **c**, Summary of results.

As predicted from the theories of the brownian motor, the efficiency of the monomeric KIF1A movement was very low. The mechanical force and work by a single KIF1A are only 0.15 pN and $\sim 0.1 k_B T$, respectively, ~0.4% of the free-energy change of ATP hydrolysis ($\sim 25 k_B T$). With the clustering of a few KIF1A molecules on the bead surface, the bead moved at ~800 nm s^{-1} up to ~2.5 pN load force (Supplementary Information 2). This enhancement is also explained by the same theory of the brownian motor[20]. The increase in the efficiency and force is caused by suppression of the diffusive movement of each head by the mechanical link to other heads (Supplementary Information 6). The putative chemical coordination between the two heads[21] and the structural change at the neck linker[3,12] further increases the efficiency and force. The observed directional binding (Fig. 3c, step 4) reflects the mechanism that enables the leading head to bind to the forward tubulin subunit but not to the backward subunit during the hand-over-hand walking of the two-headed kinesin to ensure efficient work. Furthermore, the structural similarities between kinesin, myosin and G proteins indicate that the energetic strategies and the asymmetrical binding for movement or signal transduction might be universal. This would also provide suggestions for the design principles of artificial nanomachines. □

Methods

Preparation of KIF1A beads

The design, purification and basic characterization of the KIF1A proteins are described in Supplementary Information 1. Latex beads 0.2 μm in diameter were coated with streptavidin or the F(ab') fragment of the anti-His-tag antibody[22,23]. After incubation with KIF1A for 1–4 h, the bead was diluted with buffer (Supplementary Information 1) immediately before the measurement. A custom-made optical trapping apparatus[10] was used to measure the movement of the KIF1A bead on the polarity-marked microtubule[24] attached to the coverglass. All assays were performed at 25–27 °C.

Data analysis

Bead displacements were recorded at a sampling rate of 20 kHz with a bandwidth of 10 kHz. The force of KIF1A was calculated from the bead displacement multiplied by the trap stiffness (6 fN nm^{-1}), which was determined from the variance of the thermal fluctuations of a trapped bead by the equipartition theorem of energy[11].

For analysis of the force–velocity relationship, the traces of the bead movement were segmented with a time window that was double the ATPase cycle time. The mean velocity and mean load force were calculated and scored for each segment.

Steps were detected as a rapid (less than 20 ms) positional change (more than 4 nm) followed by a long dwell (more than 10 ms) from the Harr wavelet-filtered trace[25]. Pre-step and post-step positions of the bead were calculated by averaging the raw displacement data. The step size was estimated from the difference between the pre-step and post-step positions. The mean force level was determined as the load force at the middle of the step (the mean of the pre-step and post-step positions). The dwell time was determined as the interval from one step to the next. The dwell followed by the detachment or by the more than 100-nm step back to the zero position was excluded from the statistics. The stepping time was estimated by fitting the raw data to a sigmoid curve:

$x_0 + d/\{1 + \exp[-4(t - t_0)/\tau]\}$, where x_0, d and τ denote the pre-step position, the step size and the stepping time, respectively (Fig. 2b, inset). Only steps larger than 20 nm were analysed, for accuracy in measurement of the stepping time.

For ensemble averaging, the binding events were automatically detected by thresholding the variance of the bead position (10-ms time window), and were synchronized at the decrease in the variance (green lines in Fig. 3a). Only binding events whose duration was longer than 250 ms and which were followed by the stepping movement were analysed ($n = 1,649$). The mean displacement (50-ms time window) from the averaged pre-binding position was fitted with a sigmoidal bump followed by a linear displacement: $d/\{1 + \exp(-4t/\tau)\} + vt$; $v = 0$ ($t < 0$), v_0 ($t \geq 0$). As a control, the non-specific binding of the bead to the coverglass in the absence of microtubules was analysed similarly ($n = 1,420$).

Received 21 February; accepted 19 May 2003; doi:10.1038/nature01804.

1. Hua, W., Chung, J. & Gelles, J. Distinguishing inchworm and hand-over-hand processive kinesin movement by neck rotation measurements. *Science* **295**, 844–848 (2002).
2. Kaseda, K., Higuchi, H. & Hirose, K. Coordination of kinesin's two heads studied with mutant heterodimers. *Proc. Natl Acad. Sci. USA* **99**, 16058–16063 (2002).
3. Rice, S. *et al.* A structural change in the kinesin motor protein that drives motility. *Nature* **402**, 778–784 (1999).
4. Gilbert, S. P., Moyer, M. L. & Johnson, K. A. Alternating site mechanism of the kinesin ATPase. *Biochemistry* **37**, 792–799 (1998).
5. Okada, Y., Yamazaki, H., Sekine Aizawa, Y. & Hirokawa, N. The neuron-specific kinesin superfamily protein KIF1A is a unique monomeric motor for anterograde axonal transport of synaptic vesicle precursors. *Cell* **81**, 769–780 (1995).
6. Hirokawa, N. Kinesin and dynein superfamily proteins and the mechanism of organelle transport. *Science* **279**, 519–526 (1998).
7. Okada, Y. & Hirokawa, N. Mechanism of the single-headed processivity: diffusional anchoring between the K-loop of kinesin and the C terminus of tubulin. *Proc. Natl Acad. Sci. USA* **97**, 640–645 (2000).
8. Okada, Y. & Hirokawa, N. A processive single-headed motor: Kinesin superfamily protein KIF1A. *Science* **283**, 1152–1157 (1999).
9. Tomishige, M., Klopfenstein, D. R. & Vale, R. D. Conversion of Unc104/KIF1A kinesin into a processive motor after dimerization. *Science* **297**, 2263–2267 (2002).
10. Nishiyama, M., Muto, E., Inoue, Y., Yanagida, T. & Higuchi, H. Substeps within the 8-nm step of the ATPase cycle of single kinesin molecules. *Nature Cell Biol.* **3**, 425–428 (2001).
11. Nishiyama, M., Higuchi, H. & Yanagida, T. Chemomechanical coupling of the forward and backward steps of single kinesin molecules. *Nature Cell Biol.* **4**, 790–797 (2002).
12. Kikkawa, M. *et al.* Switch-based mechanism of kinesin motors. *Nature* **411**, 439–445 (2001).
13. Block, S. M., Goldstein, L. S. & Schnapp, B. J. Bead movement by single kinesin molecules studied with optical tweezers. *Nature* **348**, 348–352 (1990).
14. Endow, S. A. & Higuchi, H. A mutant of the motor protein kinesin that moves in both directions on microtubules. *Nature* **406**, 913–916 (2000).
15. Svoboda, K., Schmidt, C. F., Schnapp, B. J. & Block, S. M. Direct observation of kinesin stepping by optical trapping interferometry. *Nature* **365**, 721–727 (1993).
16. Kikkawa, M., Okada, Y. & Hirokawa, N. 15 Å resolution model of the monomeric kinesin motor, KIF1A. *Cell* **100**, 241–252 (2000).
17. Veigel, C. *et al.* The motor protein myosin-I produces its working stroke in two steps. *Nature* **398**, 530–533 (1999).
18. Hackney, D. D. Pathway of ADP-stimulated ADP release and dissociation of tethered kinesin from microtubules. Implications for the extent of processivity. *Biochemistry* **41**, 4437–4446 (2002).
19. Astumian, R. D. Thermodynamics and kinetics of a Brownian motor. *Science* **276**, 917–922 (1997).
20. Julicher, F., Ajdari, A. & Prost, J. Modeling molecular motors. *Rev. Mod. Phys.* **69**, 1269–1281 (1997).
21. Farrell, C. M., Mackey, A. T., Klumpp, L. M. & Gilbert, S. P. The role of ATP hydrolysis for kinesin processivity. *J. Biol. Chem.* **277**, 17079–17087 (2002).
22. Berliner, E., Young, E. C., Anderson, K., Mahtani, H. K. & Gelles, J. Failure of a single-headed kinesin to track parallel to microtubule protofilaments. *Nature* **373**, 718–721 (1995).
23. Inoue, Y. *et al.* Movements of truncated kinesin fragments with a short or an artificial flexible neck. *Proc. Natl Acad. Sci. USA* **94**, 7275–7280 (1997).
24. Howard, J. & Hyman, A. A. Preparation of marked microtubules for the assay of the polarity of microtubule-based motors by fluorescence microscopy. *Methods Cell Biol.* **39**, 105–113 (1993).
25. deCastro, M. J., Fondecave, R. M., Clarke, L. A., Schmidt, C. F. & Stewart, R. J. Working strokes by single molecules of the kinesin-related microtubule motor ncd. *Nature Cell Biol.* **2**, 724–729 (2000).

Supplementary Information accompanies the paper on **www.nature.com/nature**.

Acknowledgements We thank T. J. Mitchison for the gift of GMPCPP; H. Fukuda, H. Sato and M. Sugaya for technical and secretarial assistance; and J. Howard, M. Kikkawa and our colleagues for discussion. This work was supported by a Center of Excellence Grant-in-Aid (N.H.) and a Grant-in-Aid (H.H.) from the Ministry of Education, Culture, Sports, Science and Technology of Japan.

Competing interests statement The authors declare that they have no competing financial interests.

Correspondence and requests for materials should be addressed to N.H. (hirokawa@m.u-tokyo.ac.jp).

The EMBO Journal Vol. 22 No. 19 pp. 4968–4979, 2003

Single-molecule imaging of cooperative assembly of γ-hemolysin on erythrocyte membranes

Vananh T.Nguyen[1], Yoshiyuki Kamio[1,2] and Hideo Higuchi[2,3,4]

[1]Department of Microbial Biotechnology, Graduate School of Agricultural Science, Tohoku University, Sendai 981-8555, [2]Center for Interdisciplinary Research and [3]Department of Metallurgy, Graduate School of Engineering, Tohoku University, Sendai 980-8579, Japan

[4]Corresponding author
e-mail: higuchi@material.tohoku.ac.jp

Single-molecule fluorescence imaging was used to investigate assembly of *Staphylococcus aureus* LukF and HS monomers into pore-forming oligomers (γ-hemolysin) on erythrocyte membranes. We distinguished the hetero-oligomers from the monomers, as indicated by fluorescence resonance energy transfer between different dyes attached to monomeric subunits. The stoichiometry of LukF (donor) and HS (acceptor) subunits in oligomers was deduced from the acceptor emission intensities during energy transfer and by direct acceptor excitation, respectively. Based on populations of monomeric and oligomeric intermediates, we estimated 11 sequential equilibrium constants for the assembly pathway, beginning with membrane binding of monomers, proceeding through single pore oligomerization, and culminating in the formation of clusters of pores. Several stages are highly cooperative, critically enhancing the efficiency of assembly.

Keywords: association constants/cell membranes/oligomeric intermediates/pore assembly/single-FRET

Introduction

Assembly of large macromolecular complexes such as membrane channels and cytoskeletal elements is essential for cell function. A crucial problem of protein complex assembly is to understand mechanisms of assembly processes by elucidating information on the beginning, intermediate and final stages involved (Alberts *et al.*, 2002). Heterogeneous populations of intermediate states, however, are not readily analyzed using ensemble-averaged data. In contrast, single-molecule imaging methods provide direct information about individual intermediate states (Funatsu *et al.*, 1995; Ishijima *et al.*, 1998; Schütz *et al.*, 2000). Recently, individual protein–protein interactions at very low concentrations have been observed *in vitro* under total internal reflection fluorescence microscopy (TIRF microscopy) (Mendelsohn *et al.*, 1999; Taguchi *et al.*, 2001). At high concentrations of proteins, however, dimers cannot be distinguished from crowded monomers using these techniques. Fluorescence resonance energy transfer (FRET) between single pairs of acceptor and donor fluorophores (single-FRET) has allowed observation of the dimerization even at high concentrations because the acceptor only emits fluorescence if located within several nanometers of the donor (Ha *et al.*, 1996; Sako *et al.*, 2000; Ha, 2001). Oligomers consisting of more than two molecules are also of great interest in protein assembly, although they have not been analyzed yet using single-molecule imaging.

Pore-forming toxins of bacteria are excellent models for studying the nature of assembly for oligomeric molecules on membranes because of the high stability of recombinant monomeric subunits in solution (Olson *et al.*, 1999; van der Goot, 2001). *Staphylococcus aureus* leukocidin fast fraction (LukF) and γ-hemolysin second component (HS) are water-soluble proteins that assemble into hetero-oligomeric pores of γ-hemolysin on membranes of human red blood cells (Tomita and Kamio, 1997). Using the powerful single-FRET method, hetero-oligomeric toxins consisting of two distinct components are more advantageous to study than homo-oligomeric toxins because the individual components can be treated as specific fluorescence donors and acceptors, respectively. The crystal structure of LukF monomer in solution and the pore structures observed by electron microscopy suggest beginning and ending stages of pore assembly. Nevertheless, an HS structure is not yet available, and little information about intermediates has been reported so far (Olson *et al.*, 1999; Nguyen *et al.*, 2002).

Here, we directly observed the assembly of single LukF and HS monomers into pore-forming oligomers on erythrocyte membranes under the TIRF microscope. As LukF and HS lack cysteine residues, we created single-cysteine LukF and HS mutants which are specifically labeled with donor and acceptor dyes, respectively. We developed a method to calculate the number of subunits in individual oligomers based on the intensity of FRET and direct acceptor signals. We distinguished multiple species of intermediate oligomers, and measured equilibrium association constants of sequential intermediate stages. Equilibrium constants associated with several of the stages were much higher than others, indicating cooperative assembly which resulted in great numbers of pores formed on the membranes.

Results

Fluorescence labeled proteins and model of pore assembly

We designed single-cysteine mutants of LukF (S45C) and HS (K222C) in which introduced cysteines were located on the top of the respective cap domains (Figure 1A). Fluorophore-labeled LukF-S45C–TMR (LukF–TMR) and HS-K222C–IC5 (HS–IC5) were purified with labeling degrees of >95% and were almost free of unbound dyes (Figure 1B). Hemolytic activity of the labeled mutants was

Published by Oxford University Press

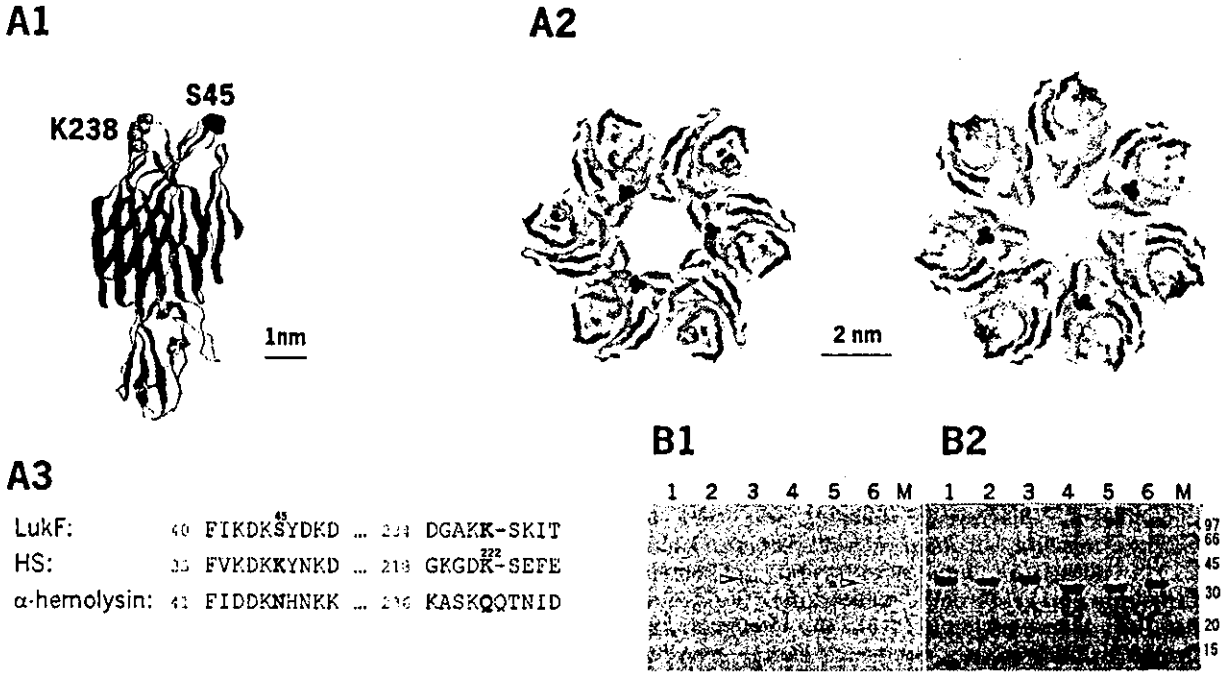

Fig. 1. Structures and labeling of LukF and HS. (A) S45 (blue) of LukF and K222 (yellow) of HS (corresponding to K238 of LukF) were mutated to Cys, shown using the LukF structure (A1), the modelled γ-hemolysin complex in hexamers or heptamers (A2), and the amino acid sequence alignment between LukF, HS, and α-hemolysin (A3). (B) SDS–PAGE gels of 10 μg of fluorescently labeled proteins, unstained (B1) and stained (B2) with Coomassie brilliant blue. Samples included: lane 1, LukF treated with TMR-maleimide; lane 2, LukF-S45C; lane 3, LukF–TMR (arrowhead); lane 4, HS treated with IC5-maleimide; lane 5, HS-K222C; and lane 6, HS–IC5 (arrowhead).

the same as that of wild-type proteins [LukF (3 nM) and HS (30 nM) caused 50% hemolysis against 6×10^{10} HRBC/l], indicating that fluorophore labeling of both mutants did not inhibit membrane binding and pore oligomerization. We detected sequential stages beginning with the binding of monomers to the membranes, then the assembly of dimers, small oligomers and single pores, and finally the formation of clusters of pores, and measured their equilibrium constants as described in the following results (Figure 6B).

Cooperative binding of HS in the presence of LukF

We verified binding constants (K_F, K_H) and the number of binding sites per μm² of erythrocyte membranes (R_F, R_H) for individual components. Concentrations of LukF–TMR or HS–IC5 bound to the membranes ($[F_b]$, $[H_b]$) were estimated by subtracting the free, unbound protein in the supernatant from the initial protein concentration ($[F_o]$, $[H_o]$) applied to a significant number of cells (e.g. 6×10^8 or 6×10^{10} cells/l). The concentrations of initial and unbound proteins were measured using a spectrofluorometer (Okada and Hirokawa, 1999). Both components quickly bound to the membranes, giving the same levels at 1 and 30 min, confirming that the standard incubation time of 10 min is long enough for equilibrium binding of LukF or HS. K_F, R_F, K_H and R_H were calculated from the fitted curves shown in Figure 2A. LukF bound strongly to membranes with a K_F of 2.1×10^{-4} μm² and a large number of binding sites (R_F) of 2.0×10^4 μm^{-2}. In contrast, a lower binding constant (K_H, 1.2×10^{-5} μm²) combined with a similar number of binding sites (R_H, 1.8×10^4 μm^{-2}) indicated a 15-fold decrease in the extent of binding of HS compared with that of LukF.

The binding ability of one component in the presence of the other was also determined. At a given $[F_o]$, $[F_b]$ slightly increased even in the presence of HS at 5-fold higher concentrations than LukF (Figure 2B1). Meanwhile the binding of HS was obviously enhanced by LukF: $[H_b]$ at a given $[H_o]$ was increased with $[F_o]$. With the same $[F_o]$ and $[H_o]$, HS bound ~4 times more than it did without LukF (Figure 2B2). Combining all these data, we demonstrate that both LukF and HS can spontaneously bind to HRBC membranes, but with different binding constants, and that LukF obviously enhances the membrane binding of HS.

Individual monomers and dimers on the membranes

We visualized assembly of LukF–TMR and HS–IC5 on the membranes, at equilibrium, under a TIRF microscope equipped with a double-view unit to observe images simultaneously at two wavelengths, 565–595 nm (the TMR signal) and 650–690 nm (the IC5 signal) (Figure 3A). Using very low concentrations of the two proteins (75 pM LukF and 750 pM HS), at which hemolysis did not occur, Figure 3B1 and B2 show TMR and FRET-IC5 signals on the same cell, excited by the green laser. Figure 3B3 shows IC5 signals on that same cell, excited by the red laser. The spots on Figure 3B1 and B3 represent membrane-bound LukF–TMR and HS–IC5, and the spots on Figure 3B2 represent LukF–TMR assembling into oligomers with HS–IC5. Only a few punctate FRET-IC5 spots, ranging from 0 to 10, were observed on each cell.

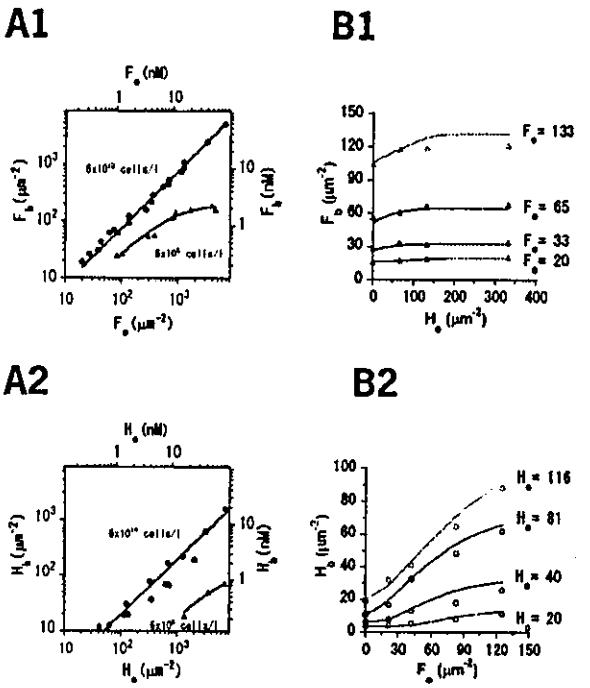

Fig. 2. Membrane binding of LukF and HS. (A) Binding of LukF–TMR (A1) or HS–IC5 (A2). $[F_b]$ or $[H_b]$ were plotted against $[F_o]$ or $[H_o]$ at 6×10^{10} (filled circles) and at 6×10^{8} (filled triangles) HRBC/l. The red lines represent the fitting of data (Appendix I). (B) Binding of both LukF–TMR and HS–IC5 to 6×10^{10} HRBC/l. At four values of $[F_o]$ (B1) and $[H_o]$ (B2), the relative $[F_b]$ and $[H_b]$ were measured in the presence of the other at different concentrations. The lines represent theoretical values of F_b (H_b), calculated based on the binding and association constants.

To calculate the numbers of LukF–TMR (m) and HS–IC5 (n) in individual FRET-IC5 oligomers (F_m·H_n), the occurrence of stepwise decays in the fluorescence intensity was measured. An acceptor (orange line at 8 s in Figure 3B4, left panel) was suddenly photobleached, and at the same time the intensity of donor was increased (green line). In another case, the donor was photobleached first (at 12 s in the right panel of Figure 3B4) as the FRET signal suddenly dropped without an increase in donor emission. This was confirmed by the fact that the acceptor signal detected by direct excitation with the red laser remained until its own photobleaching at 57 s (Figure 3B4, right panel). All of the stepwise photobleachings were classified into these two groups (acceptor photobleached first, number of spots = 31; donor photobleached first, number of spots = 14). The absence of anticorrelated fluctuations between the donor and acceptor indicated the flexible rotations of the labeled dyes during video recording (33 ms), allowing us to exclude the effect of polarization of dyes in deducing the distance between donor and acceptor from FRET efficiency. This behavior proves that single FRET spots are dimers containing one LukF and one HS (F·H).

We measured the FRET-IC5 intensity ($I_{\text{FRET-IC5}}$) and the FRET efficiency (number of spots = 45) on the dimers. $I_{\text{FRET-IC5}}$ values were well fitted in a Gaussian distribution with a mean of 0.87 ± 0.25 relative to IC5 intensities excited by the red laser. Five representative images (Figure 3B5) showed large FRET efficiencies, ranging from 72 to 100%. FRET efficiency was 87 ± 10% relative to the TMR intensity in dimers, indicating a distance between LukF–TMR and HS–IC5 in a dimer of ~4.5 nm, estimated from a Förster distance (R_0) of 5.4 nm between TMR and IC5 (R_0 between TMR and Cy5 is 5.3 nm; Ha *et al.*, 1996). This distance is consistent with predicted distances between IC5 and the two neighbouring TMR moieties, as shown in Figure 1A2.

The equilibrium association constants for dimerization $K_{F\text{·}H} = ([F\text{·}H] \times [F_1]^{-1} \times [H_1]^{-1})$ were also estimated, based on the concentrations of monomers ($[F_1] = 3.8$ and $[H_1] = 6.9\ \mu m^{-2}$) and dimers ($[F\text{·}H] = 0.026\ \mu m^{-2}$) on the cell membranes (number of cells = 37), to be 0.0010 ± 0.0003 μm^2 (Table I). In this experiment, the ghost cells were incubated with low concentrations of proteins as above, but without washing off free proteins in solution. $[F\text{·}H]$ in both the washed preparations (0.026 ± 0.004 μm^{-2}) and the non-washed ones (0.027 ± 0.008 μm^{-2}) was similar, confirming that dissociation of F·H into monomers is negligibly slow in our conditions. Therefore, in further experiments, we washed off the unbound proteins to reduce the background from monomers in FRET-IC5 detection and to analyze the oligomers more precisely.

To confirm that LukF and HS do not dimerize in solution before incubation with cells, we incubated the two components in aqueous solution at 6-fold higher concentrations than those used in the presence of cells, then observed these in the same system. However, there is no observable FRET signal, confirming that LukF and HS are monomers in solution and oligomerize only on the membranes.

To test for the possibility of homodimer oligomerization (F·F or H·H) on the membranes, we observed each individual component labeled with both dyes, that is, mixtures of LukF–TMR and LukF–IC5, or of HS–TMR and HS–IC5, on the membranes. And to test whether FRET actually is an indicator of direct interaction between the two components, a couple of mutants of LukF ($LukF_{33}$–TMR) and HS (HS_{29}–IC5) that failed to form oligomers were used as a negative control for FRET. In both cases, no FRET-IC5 was detected even at concentra-

Fig. 3. Visualization of small oligomers of LukF and HS. (A) Arrangement of the TIRF microscope for observation of oligomerization on the membranes (A1). Fluorescence signals near the basal membrane appeared on the double-view monitor: the left is for the donor, the right is for FRET and the acceptor (A2). (B and C) Images of dimers formed by LukF–TMR and HS–IC5 on HRBC membranes at low concentrations of proteins (75 and 750 pM, respectively) (B1–B3), and at higher concentrations of LukF–TMR (300 pM) and lower HS–IC5 (200 pM) (C1–C3). TMR, FRET and IC5 signals are shown after excitation by the green laser (B1 and B2; C1 and C2; time 0), and by the red laser (B3 and C3; time 0), respectively. B4 shows time traces of TMR (green), FRET (orange) and IC5 (red) emission corresponding to dimers (F·H = LukF–TMR HS–IC5). The left trace (eight frame-averaged) indicates that IC5 photobleaches first, and the right trace (30 ms interval) indicates that TMR photobleaches first. Five images of dual signals of TMR and FRET acquired from the same spots (B5). Thirty millisecond interval time traces of acceptor emission on anticorrelated excitation by the green and red lasers for short (~3 s) or long times (>10 s), showing trimers (F_2·H_1; C4) and tetramers ($(F\text{·}H)_2$; C5).

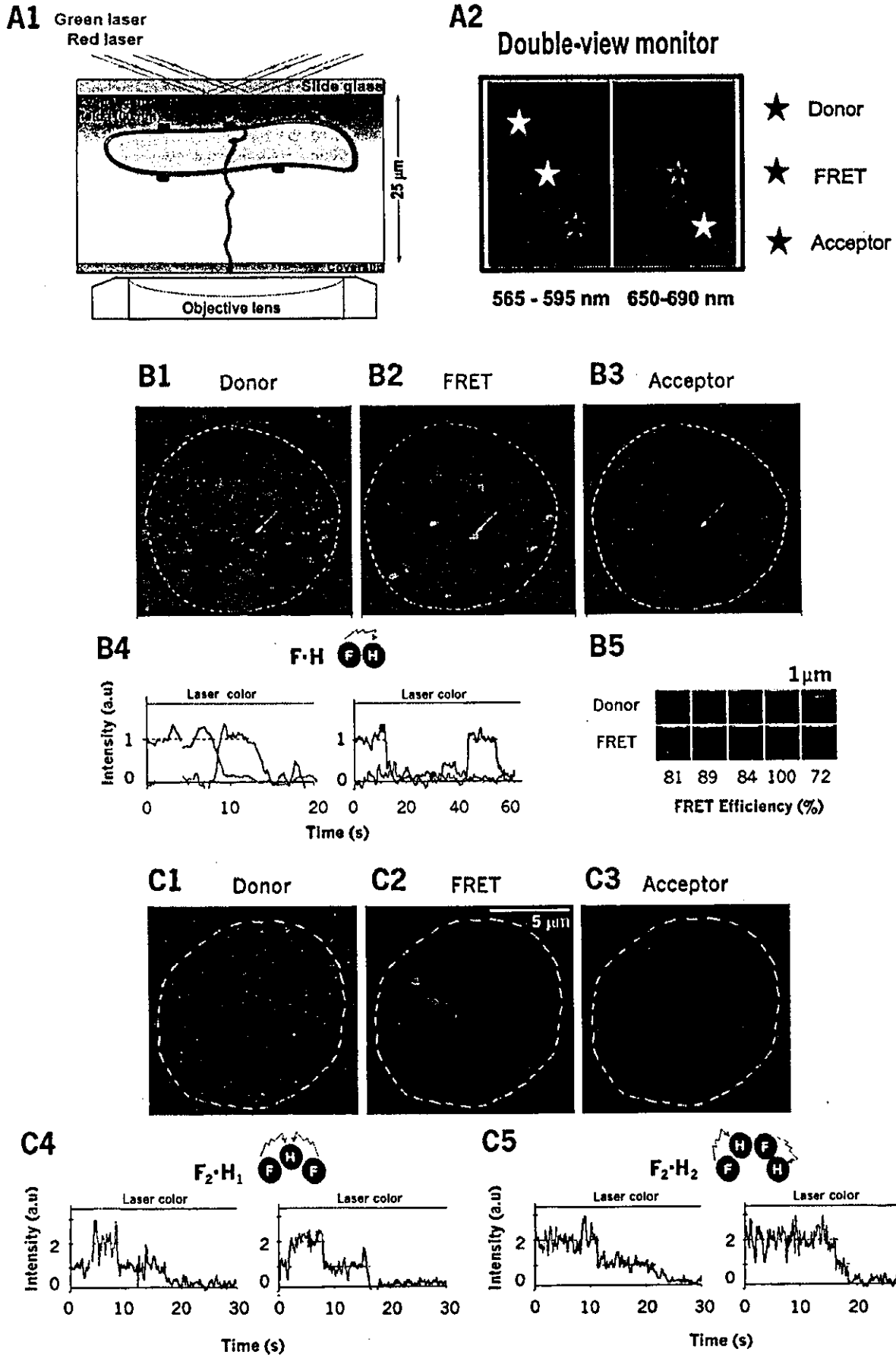
A1
Green laser
Red laser
Slide glass
25 μm
Objective lens
A2
Double-view monitor
Donor
FRET
Acceptor
565 - 595 nm
650-690 nm
B1
Donor
B2
FRET
B3
Acceptor
B4
F·H
Laser color
Laser color
Intensity (a.u)
Time (s)
B5
1μm
Donor
FRET
81 89 84 100 72
FRET Efficiency (%)
C1
Donor
C2
FRET
5 μm
C3
Acceptor
C4
F2·H1
Laser color
Laser color
Intensity (a.u)
Time (s)
C5
F2·H2
Laser color
Laser color
Intensity (a.u)
Time (s)

tions 6-fold higher than those used for the heterodimer of LukF–TMR and HS–IC5, confirming that only the LukF and HS couple have a high affinity for direct interaction to form oligomers on the membranes.

Tetramerization: the dimer–dimer interaction

To achieve assembly of LukF and HS into dimers and other small oligomers, the concentration of LukF (Figure 3C) was increased to four times that of Figure 3B, and the concentration of HS–IC5 monomers was decreased. Most of the individual FRET intensities were equal to or twice the value of the single-FRET intensities measured in Figure 3B. The FRET-IC5 intensity of oligomers should be proportional to the number of donors if the acceptors are close to the donors and excitations of two or more donors do not overlap due to the low excitation power of the green laser (Lakowicz, 1999). The requirement for close distances between the acceptors and neighbouring donors is likely met, as supported by the evidence that single HS–IC5 absorbed nearly 90% of the energy emitted by single LukF–TMR within dimers. The FRET intensity of heterodimers was proportional to the intensity of the green laser up to 10 times higher than our standard illumination, indicating that the excitations of the donors did not overlap under our condition. m and n in $F_m{\cdot}H_n$ were deduced from the number of steps observed during photobleaching of FRET-IC5 (orange lines) and IC5 signals (red lines), respectively (Figure 3C4 and C5). The left panel of Figure 3C4 shows representative photobleaching steps of trimers: single IC5 intensity on excitation by the red laser up to 2 s indicates a single HS (H_1). Then, on switching to the green laser, the intensity of the FRET-IC5 signal doubled, indicating the presence of two molecules of LukF (F_2). Switching back to the red laser at ~15 s caused the single photobleaching of HS–IC5, confirming H_1. Similarly, dimers, trimers and teteramers were characterized and shown in representative images and profiles of FRET and acceptor intensities, such as $F{\cdot}H$ (Figure 3C2), $F_2{\cdot}H_1$ (Figure 3C4), $F_1{\cdot}H_2$ (data not shown), and $(F{\cdot}H)_2$ (Figure 3C5).

A tetramer could be formed by two pathways: (i) tetramerization of two dimers [$F{\cdot}H + F{\cdot}H \rightarrow (F{\cdot}H)_2$] or (ii) 'step-by-step' oligomerization of monomers [$F{\cdot}H + F \rightarrow F_2{\cdot}H_1 + H \rightarrow (F{\cdot}H)_2$ or $F{\cdot}H + H \rightarrow F_1{\cdot}H_2 + F \rightarrow (F{\cdot}H)_2$]. To test which is the main pathway, we measured the association constants for each stage from the concentrations of oligomeric intermediates ($K_{F2{\cdot}H}$, $K_{F{\cdot}H2}$ and $K_{(F{\cdot}H)2}$ in Table I; Appendix 2). In observations from 20 cells (number of spots = 104), even though $[F_1]$ was ~10–35 times higher than $[H_1]$, the number of $F_2{\cdot}H_1$ complexes was almost equal to that of $(F{\cdot}H)_2$ complexes, and much fewer than the number of $F{\cdot}H$ heterodimers, indicating that monomers prefer to oligomerize into dimers and tetramers rather than into trimers. Association constants for 'dimer–dimer' tetramerization, $K_{(F{\cdot}H)2} = 3.8\ \mu m^2$, were >30 times those for the step-by-step processes, $K_{F2{\cdot}H} = 0.081\ \mu m^2$ and $K_{F{\cdot}H2} = 0.12\ \mu m^2$. This result could be interpreted as the step-by-step pathway being of far less significance than the dimer–dimer pathway. Moreover, we did not find any spot corresponding to $F_3{\cdot}H_1$ or $F_4{\cdot}H_1$, confirming that the complementary side-by-side interaction between LukF and HS is specific for dimerization and that oligomers containing multiple $F{\cdot}H$ pairs are stable.

Assembly into a single pore: a cooperative step

To analyze the next oligomerization steps, we raised the concentrations of both proteins so that various intermediates from dimers to larger oligomers could be obtained (Figure 4). Figure 4A2 shows various intense spots scattered on the membrane. Individual FRET intensities were ~1, ~2 and ~3 times the single-FRET intensity of $F{\cdot}H$ (Figure 4A2 and B). The multi-FRET efficiencies of representative spots was also ~90% (Figure 4C), indicating a close distance between LukF and HS components in larger oligomers.

Because the major pathway for tetramerization was via dimer–dimer interaction, the spots at relative intensities of ~2 should be tetramers consisting of pairs of dimers. Considering heterodimers to be of high stability, the spots at an intensity of ~3 could be resolved as hexamers of three heterodimers. However, it is also possible to resolve these spots as heptamers consisting of 3F and 4H because the FRET-IC5 intensity of oligomers is proportional to the number of donors if the acceptors are close to the donors.

Table I. Binding and association constants of intermediate stages in the pore assembly pathway

Data in Figures	Constants		Concentrations of monomeric and oligomeric intermediates (μm^{-2})		
2A	K_μ	2.1×10^{-4}			
	K_H	1.2×10^{-5}			
	R_F	2.0×10^{4}			
	R_H	1.8×10^{4}			
3B	$K_{F{\cdot}H}$	0.0010 ± 0.0003	$[F_1] = 3.8 \pm 0.6$	$[H_1] = 6.9 \pm 1.1$	$[F{\cdot}H] = 0.026 \pm 0.004$
3C	$K_{F2{\cdot}H}$	0.081 ± 0.032	$[F_1] = 3.75 \pm 0.05$	$[F{\cdot}H] = 0.056 \pm 0.006$	$[F_2{\cdot}H_1] = 0.017 \pm 0.003$
	$K_{F{\cdot}H2}$	0.12 ± 0.084	$[H_1] = 0.27 \pm 0.02$	$[F{\cdot}H] = 0.056 \pm 0.006$	$[F_1{\cdot}H_2] = 0.0017 \pm 0.0012$
	$K_{F2{\cdot}H2}$	3.82 ± 1.23	$[F{\cdot}H] = 0.056 \pm 0.006$	$[F{\cdot}H] = 0.056 \pm 0.006$	$[F_2{\cdot}H_2] = 0.012 \pm 0.003$
4	$K_{F2{\cdot}H2}$	3.1 ± 1.1	$[F{\cdot}H] = 0.065 \pm 0.0092$	$[F{\cdot}H] = 0.065 \pm 0.0092$	$[F_2{\cdot}H_2] = 0.013 \pm 0.0041$
	K_p	37 ± 14	$[F{\cdot}H] = 0.065 \pm 0.0092$	$[F_2{\cdot}H_2] = 0.013 \pm 0.0041$	$[F_3{\cdot}H_3] = 0.032 \pm 0.0063$
5A and B	K_{2p}	1.1 ± 0.22	$[F_3{\cdot}H_3] = 0.24 \pm 0.019$	$[F_3{\cdot}H_3] = 0.24 \pm 0.019$	$[F_6{\cdot}H_6] = 0.066 \pm 0.010$
	K_{3p}	2.7 ± 0.68	$[F_3{\cdot}H_3] = 0.24 \pm 0.019$	$[F_6{\cdot}H_6] = 0.066 \pm 0.010$	$[F_9{\cdot}H_9\ ] = 0.043 \pm 0.0080$
	K_{4p}	3.4 ± 1.1	$[F_3{\cdot}H_3] = 0.24 \pm 0.019$	$[F_9{\cdot}H_9] = 0.043 \pm 0.0080$	$[F_{12}{\cdot}H_{12}] = 0.035 \pm 0.0075$
6A	K_{np}	3.0			

Binding and association constants are in units of μm^2; numbers of binding sites (R_F, R_H) are in μm^{-2}. Values are given as mean ± error, where error = mean × $n^{-0.5}$, and n is the number of measured spots. The values were calculated from the equations described in the Appendix.

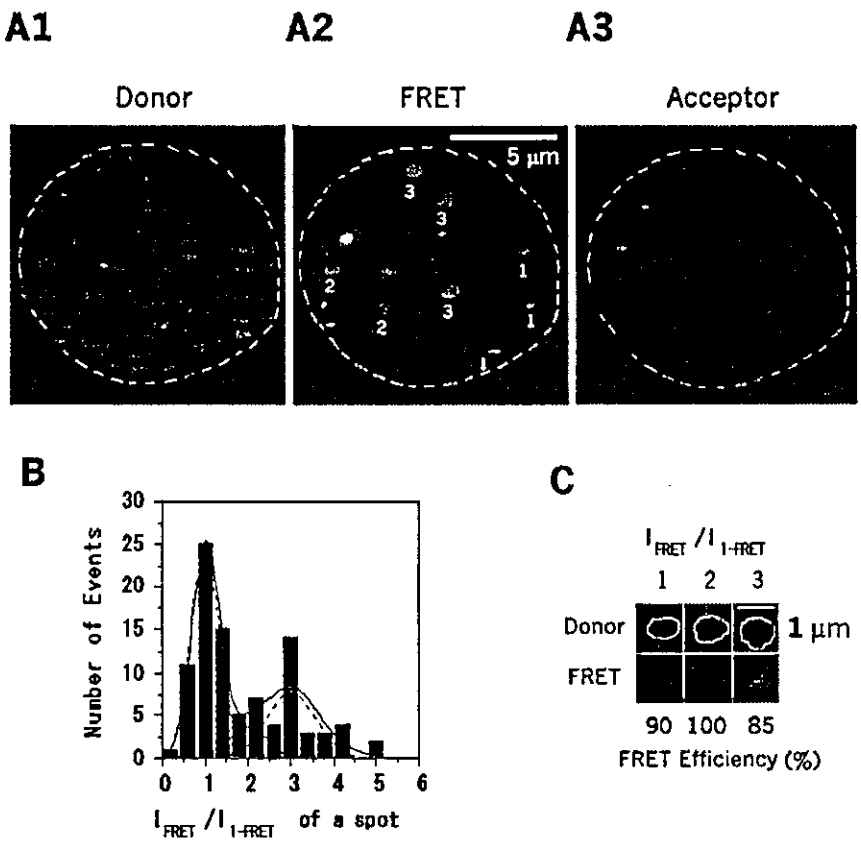

Fig. 4. Visualization of intermediate oligomers and single pores. LukF–TMR and HS–IC5 were incubated with HRBC at intermediate concentrations of 400 pM and 4 nM, respectively. (A) TMR (A1; time 0), FRET (A2; time 0) and IC5 signals (A3; time 44 s) are on the same cell. White numbers on A2 indicate m in $F_m{\cdot}H_n$. (B) Population histogram of intermediate oligomers: the dashed and solid lines indicate Gaussian distribution peaks for $F{\cdot}H$, $(F{\cdot}H)_2$, $F_3{\cdot}H_{3-4}$ and for the total population, respectively. (C) Three images of dual signals of TMR and FRET-IC5, showing single and multi-molecule FRET efficiencies between LukF–TMR and HS–IC5 in dimers and larger oligomers.

For statistical analysis, the histogram of FRET intensities was fitted as the sum of three Gaussian distribution curves (Figure 4B). The spots at intensity ~3 were more abundant than those at ~2, and ~4. Since the ratio of initial concentrations of F:H applied to the cells is 1:10, the population of spots at intensity ~4 presenting heptamers of 4F:3H were low. The possible octameric formation of 4F:4H also appeared minor. Assuming the area under each Gaussian curve is proportional to the number of oligomers, $F{\cdot}H$, $(F{\cdot}H)_2$ and $F_3{\cdot}H_{3-4}$, we estimated sequential association constants $K_{(F{\cdot}H)2}$, and $K_{F3{\cdot}H3-4}$ to be 3.1 and 37 μm^2, respectively (Table I). As single γ-hemolysin pores have been reported as hexamers and/or heptamers (Sugawara *et al.*, 1997; Comai *et al.*, 2002; Sugawara-Tomita *et al.*, 2002), $K_{F3{\cdot}H3-4}$ was assigned as the association constant for single a pore, K_p. Obviously, K_p was more than 10 times higher than $K_{(F{\cdot}H)2}$, suggesting that LukF prefers assembling with HS into hexameric and/or heptameric pores $F_3{\cdot}H_{3-4}$ rather than into tetramers $(F{\cdot}H)_2$.

Assembly into clusters of pores

The final experiment was conducted to analyze distributions of large oligomers by increasing concentrations of LukF–TMR and HS–IC5 to achieve 15–100% hemolysis. At higher concentrations (~15% hemolysis), we lowered the excitation powers of the green and red lasers by 25% to stay within the linear intensity range of the camera. This resulted in an ability to resolve FRET signals of about twice the value of single-FRET. Therefore, we could reliably observe FRET signals which were equal to or higher than three times the single-FRET signal, corresponding to a pore. The number of pores incorporated into each FRET spot was deduced from the FRET intensity of the spot divided by three times the single-FRET intensity. The pores did not scatter randomly on the membranes but aggregated into small clusters consisting of 2–3 pores, as estimated from the intensity of the spots (Figure 5A2). The occurrence of single pores and clusters on the membranes was plotted as a histogram in Figure 5B, indicating that single pores were abundant compared to clusters of pores. Association constants of single pores into two (K_{2p}), three (K_{3p}) and four pores (K_{4p}) were 1.1, 2.7 and 3.4 μm^2, respectively, as shown in Table I. Those increasing values indicate that single pores tend to assemble into 3-pore or 4-pore clusters rather than into 2-pore clusters.

When LukF–TMR and HS–IC5 were increased over the concentrations that start causing 100% hemolysis (Figure 5C), the power of the green excitation was reduced to 2.5%. Very highly intense domains of multi-molecular FRET-IC5, probably clusters of pores, could be observed.

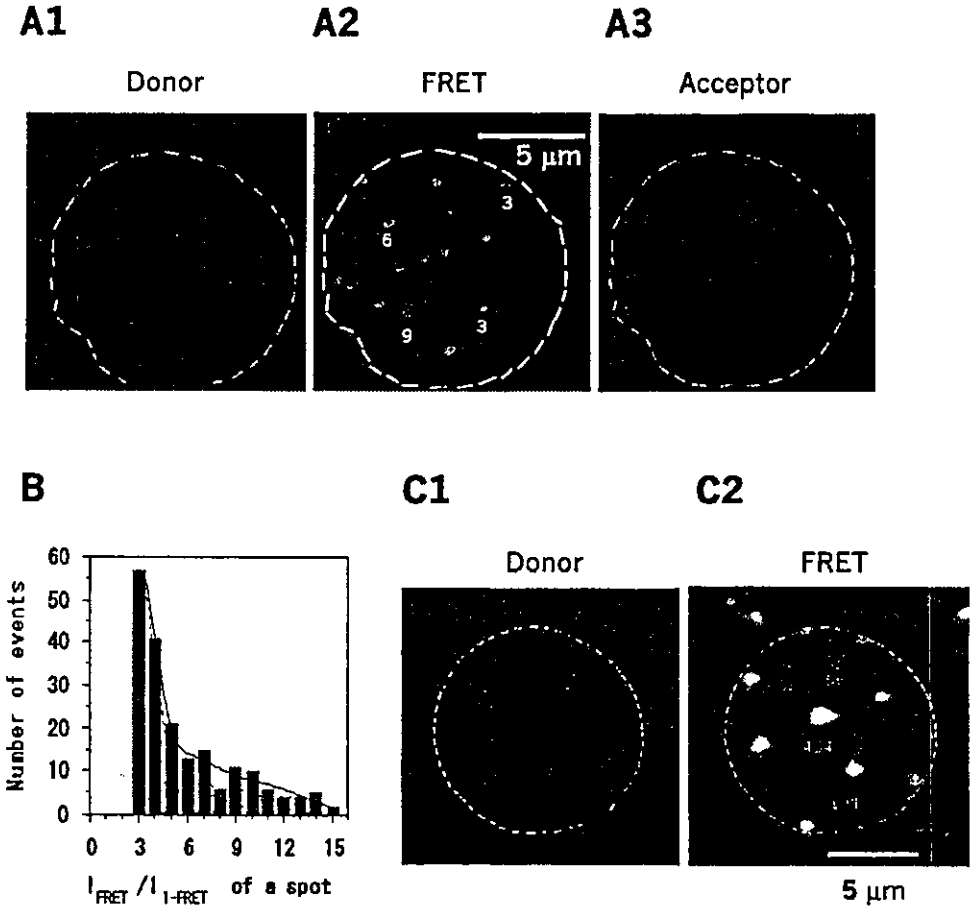

Fig. 5. Visualization of clusters of pores. LukF–TMR and HS–IC5 were incubated with HRBC at high concentrations of 1.5 and 15 nM (A), or of 15 and 150 nM (C), respectively. LukF–TMR and HS–IC5 were excited by two lasers at 25% power (A), and at 2.5% power (C), compared to that used for single FRET observation. TMR (A1 and C1) and FRET (A2 and C2) signals show clusters of pores scattered on the membranes. IC5 signals (A3) are on the same cell with A1, A2. White numbers on A2 indicate m in F_m·H_n. Blue numbers on C2 indicate the number of pores in each large spot. (B) Histogram of populations of F_m·H_n corresponding to single pores and groups of pores at 15% hemolysis. The dotted and solid lines indicate Gaussian distribution peaks at single, two, three and four pores, and the total population, respectively.

The domains were far from being randomly distributed on the cell, but appeared with an occurrence of 7–15 domains/cell. We plotted a distribution of clusters with various numbers of pores on the membranes in Figure 6A (blue circles). The distribution dropped gradually with the sizes of clusters. The FRET efficiency values of those domains were about 73 ± 13%. These values were slightly lower than that of single-FRET or multi-FRET of a pore, presumably due to co-localization of LukF–TMR monomers in areas of the clusters.

Calculating the population of intermediate states

Taking the four binding (K_F, K_H, R_F, R_H) and five association ($K_{F\cdot H}$, $K_{(F\cdot H)2}$, K_p, K_{2p}, K_{np}) constants (Table I; Appendix sections 2 and 3), we estimated the theoretical distribution of intermediates and the total number of pores at given concentrations of proteins. Assuming that K_{np} ($n > 2$) values are similar to K_{3p} and K_{4p} (3 μm^2), at certain [F_o] and [H_o], for example 25 and 1000 μm^{-2}, the distribution of monomers and oligomers could be calculated. At low concentrations of LukF and HS (25 mm^{-2}) close to those used in Figure 4, the calculated distribution of dimers, tetramers and single pores (Figure 6A, dotted red line) is similar to the distribution data shown in Figure 4B. The total number of pores is calculated to be $\Sigma n \times [P_n] \sim 0.036$ μm^{-2}. Using 1000 μm^{-2} each of LukF and HS (Figure 6A, red solid line), almost the same concentrations used in Figure 5C, the total concentration of pores ($\Sigma n \times [P_n]$) was ~300 μm^{-2}. Populations of clusters of pores (Figure 6A, blue circles) measured from 237 spots on cell membranes at the concentration used in Figure 5C fits well with the theoretical red line, confirming the assumption that K_{np} ($n > 2$) = 3 μm^2.

To explain the enhancement in membrane binding of HS induced by LukF, the total concentrations of HS on the membranes ([H_b]) for applied [H_o] in Figure 2B2 were calculated from the association constants in Table I. The calculated values (lines) gave a good fit to the experimental results (circles) for HS binding in the presence of LukF (Figure 2B2). At very high concentrations of LukF, most of the HS bound to the membranes. The effect of LukF on membrane binding of HS was probably due to the sequential oligomerizations that shifted the membrane

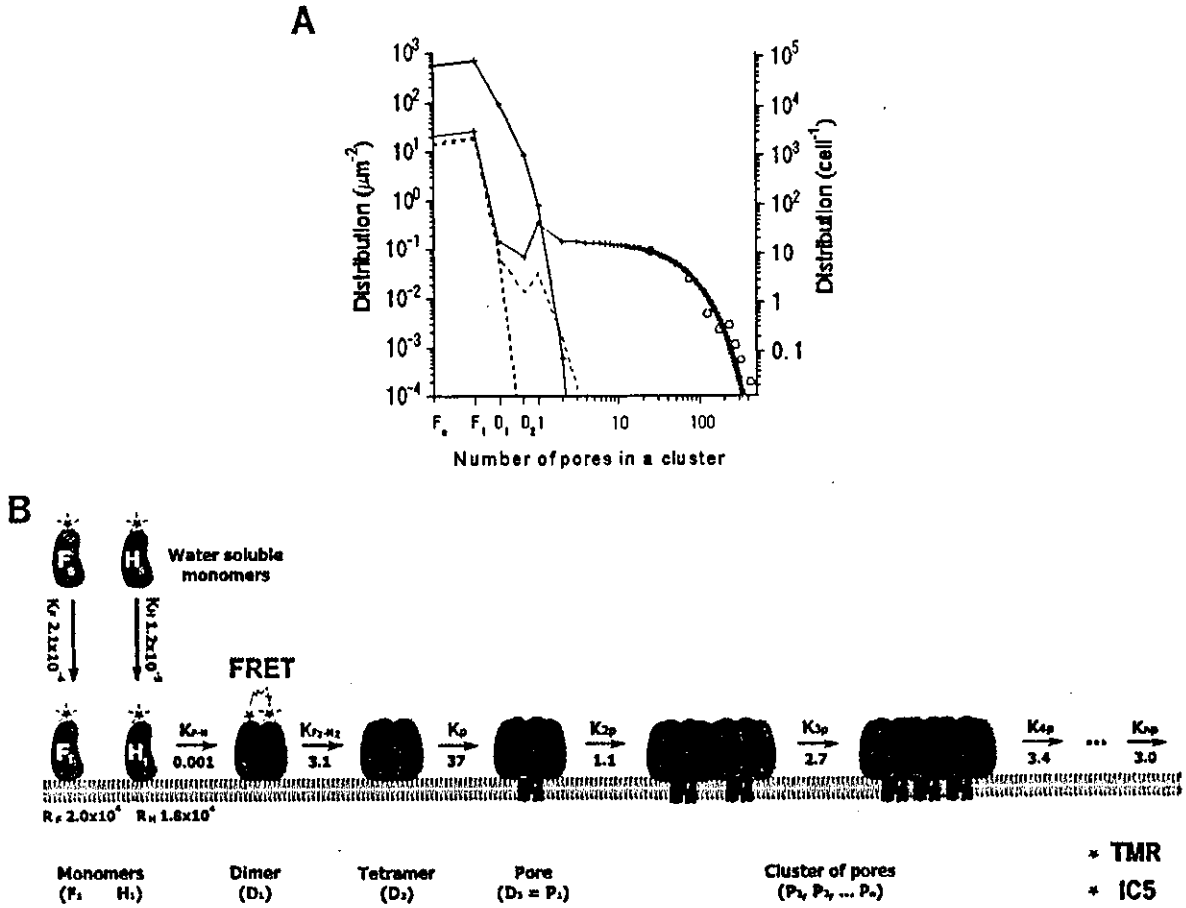

Fig. 6. Simulations and models for pore assembly. (A) Experimental and theoretical distribution of intermediates at given protein concentrations (K_{np} is assumed to be ~K_{3p} or K_{4p}). The blue circles were measured from 237 spots of data (as for Figure 5C), and were fitted by the theoretical red line. The dotted and solid lines represent theoretical distributions at $[F_o]$ and $[H_o]$ of 25 and 1000 μm^{-2}, respectively. The red lines represent a fully cooperative process, similar to natural conditions. The black lines represent non-cooperative processes (K of all stages are ~$K_{F\text{-}H}$). (B) Cartoon model for pore assembly of LukF and HS. Water-soluble LukF (green) and HS (red) monomers bind to putative binding sites on the membranes. Sequentially, the membrane-bound monomers assemble into small oligomers (e.g. dimers and tetramers), then into single pores and clusters of pores. The pore is represented as a hexamer, although formation of hexameric and/or heptameric pores is possible. The FRET signals indicate oligomers. The blue lines indicate the transmembrane domains inserting through lipid bilayers upon pore formation. The numbers indicate equilibrium binding and association constants (μm^2).

association–dissociation balance of HS in the direction of association.

Discussion

Advantages of single-FRET in the detection of intermediate oligomers

Ensemble methods such as equilibrium analytical ultracentrifugation have been used to measure concentration averages of assumed monomers, tetramers and octamers during cooperative association of an oligomeric DNA-binding protein (Daugherty *et al.*, 1999). However, the oligomers are not well separated and the concentrations of monomers required are high (μM). Transmission electron microscopy at the level of single molecules cannot allow for the observation of the oligomerization process from monomers to tetramers due to limited spatial resolution. Our single molecule observation technique offers the ability to distinguish intermediates under physiologically-relevant conditions. The FRET measurement for single and multiple molecules is effective in distinguishing oligomers from crowded monomers. Moreover, we developed a novel method to deduce the number of LukF (donor) and HS (acceptor) molecules in small oligomers, such as trimers and tetramers, by measuring the stepwise photobleaching of FRET and acceptor signals, respectively.

Cooperative assembly of monomers into oligomers

The membrane binding affinity of each component of γ-hemolysin has been unclear and controversial because of low resolution in detecting protein concentrations (1 nM) (Kaneko *et al.*, 1997; Ferreras *et al.*, 1998). Here, we demonstrate that both LukF and HS individually bind to membranes as monomers, even at 20 pM. LukF binds to membranes with a 20-fold higher affinity than does HS ($K_F = 10 \times K_H$), consistent with the data reported by Kaneko and colleagues in 1997. The higher K_F for LukF supports a previous suggestion regarding stable interactions between

aromatic amino acids of the rim domain of LukF and the phospholipid head groups on the outer membranes (Olson *et al.*, 1999). The lower K_H for HS suggests different properties of putative binding sites for HS or different membrane-binding surfaces compared with those of LukF.

At the dimerization stage, stepwise photobleaching of single-FRET in the presence of LukF–TMR and HS–IC5 on the membranes proved the existence of heterodimer $F{\cdot}H$ (Figure 3B4). However, the lack of observable FRET of the couples LukF–TMR and LukF–IC5, and HS–TMR and HS–IC5 proves that there is no possibility of $F{\cdot}F$ and $H{\cdot}H$ homodimer formation. The heterodimer $F{\cdot}H$ is formed not in solution but on the membranes because no FRET was observed in solution. The specific formation of heterodimer on the membranes may be promoted by two dimensional side-by-side collisions between LukF and HS, as confirmed by negative FRET evidence using $LukF_{33}$–TMR and HS_{29}–IC5, the point mutants at interaction surfaces lacking oligomerization ability. We suggest that structural changes of LukF or HS induced at membrane binding strengthen the side-by-side interactions between the two subunits.

Membrane-bound trimers and tetramers were observed for the first time. The abundance of dimers compared to trimers, together with the observation of similar concentrations of trimers and tetramers, even when the membrane-bound LukF monomer concentrations are ~10–35 times those of HS monomers, prove that monomers have a tendency to oligomerize into dimers and tetramers, rather than into trimers. Thus, dimer–dimer interaction is the major pathway for formation of tetramers (Figure 6B). It is possible that dimerization triggers structural changes at the interaction sides of their subunits for further cooperative tetramerization.

In the assembly of pores and clusters of pores, the required high HS concentration did not allow us to discern an HS oligomer from crowded HS monomers under direct acceptor excitation. Therefore, we were obliged to assume that the ratio of F to H in an oligomer is close to 1:1, $F_m{\cdot}H_m$ or $F_m{\cdot}H_{m+1}$, as suggested previously from stability of the multi-dimer oligomers. Concerning the subunit stoichiometry of single pores, an exact number has not been determined yet as the fine crystal structure of γ-hemolysin purified from membranes is not available. Recent reports by Comai *et al.*, and Sugawara *et al.*, respectively, suggest that six and seven subunits of LukF and HS make up a single pore (Sugawara *et al.*, 1997; Comai *et al.*, 2002; Sugawara-Tomita *et al.*, 2002). However, the latter group also observed ~25% hexameric pores in addition to the heptameric pores, suggesting the coexistence of hexamers and heptamers (N.Sugawara, T.Tomita and Y.Kamio, unpublished data). In another report, Miles *et al.* proposed an octameric structure for the staphylococcal leukocidin pore of LukF and LukS formed on lipid bilayers, based on the results obtained from gel shift electrophoresis and site-specific chemical modification during single-channel recording, but not by direct imaging (Miles *et al.*, 2002). However, their results are also consistent with the heptameric stoichiometry with 3:4 or 4:3 compositions of LukF and LukS (Sugawara-Tomita *et al.*, 2002). In view of this, we assume that the 3× single FRET spots, which could be resolved as either hexamers $(F{\cdot}H)_3$ or heptamers $F_3{\cdot}H_4$, represent single pores, and that the spots exhibiting intensity with a common multiple (n times) of three LukF molecules $(F_3{\cdot}H_{3-4})_n$ present clusters of pores. Cell lysis started occurring at the protein concentrations (Figure 4) applied, confirming that functional pores were formed, although we have not been able to correlate the 3× single-FRET spots with the direct imaging of pore opening. Actually, in modelling the pathway of pore assembly (Figure 6B), whether the pore is assumed to be composed of six or seven subunits, the further calculation of association constants and final fitting of intermediate populations (Figure 6A) are not affected because the populations of groups and clusters of pores were simply deduced based on the value of 3× single FRET. Here, the $F{\cdot}H$ dimers, $(F{\cdot}H)_2$ tetramers and $F_3{\cdot}H_{3-4}$ single pores presented major macroscopic intermediates in single pore oligomerization (Figure 6B). The high value of $K_{F3{\cdot}H3-4}$ or K_p (37 μm²) is an indicator of the cooperative assembly of subunits to generate single pores. The closed, ring-shaped structure of a pore would be very stable for minimizing the free energy at surface regions. At the pore formation step in Figure 6B, we depict the transmembrane domains (blue lines) inserting into lipid bilayers because previous data report that the transmembrane domain of LukF inserts into membranes to form a barrel-shaped channel on conversion from a pre-pore to a functional hemolytic pore (Nguyen *et al.*, 2002).

γ-hemolysin pores have a greater tendency to condense into clusters as the concentration of toxin is increased, and may assemble into ≥3 pores because K_{3p} and K_{4p} were ~3 times higher than K_{2p}. This result is supported by the previous data showing that large clusters of pores could be observed at higher concentrations of proteins (1 μM) under a transmission electron microscope (TEM) (Sugawara *et al.*, 1997). Since clusters of pores are also observed in many other toxins, even in lipid vesicles (Wallace *et al.*, 2000), we suppose that the aggregation of pores is not only driven by the distribution of their receptors on the membranes, but also by non-covalent linkages between amino acids located at the outer surfaces of the pores. One advantage of pore aggregation could be the switching of the equilibrium balance of single pore assembly toward association, thereby increasing the total number of pores per cell. The other advantage would be that large clusters of pores on the membranes weaken the cell membranes and enhance the cell bursting. Cell membranes were recently found to be prominently disrupted in areas surrounding the clusters, as observed under TEM (N.Sugawara, T.Tomita and Y.Kamio, unpublished data).

Self-assembly of macrostructures and association constants

We estimated the distributions of intermediate oligomers over a wide concentration range of toxin applied to the cells. The cooperative assemblies for tetramers, single pores and clusters of pores greatly enhance the total concentration of pores ($\Sigma n \times [P_n] \approx 300\ \mu m^{-2}$) up to ~$2.5 \times 10^5$ times of that in a non-cooperative assembly ($\Sigma n \times [P_n] \approx 0.0122\ \mu m^{-2}$) for which the assembly for all stages is assumed to be ~$K_{F{\cdot}H}$ of 0.0010 μm² (Figure 6, black solid line). Such overall cooperativity is, indeed, critical for γ-hemolysin to burst the erythrocytes in a human body at low concentrations of the toxin. With this new understanding of the cooperative assembly, we may

interfere with the toxicity of γ-hemolysin by suppressing cooperative stages. For example, a chemical reagent that binds specifically to an interaction surface of either LukF or HS could effectively inhibit tetramerization and pore formation.

Other toxins from pathogenic bacteria, such as aerolysin, streptolysin and perfringolysin O which form homo-oligomeric pores on human target cell membranes (van der Goot, 2001), may also cooperatively assemble in a mechanism similar to that of γ-hemolysin. Outside of the toxin field, there are many kinds of ring-shaped membrane channels and pumps made up of multiple subunits. Selective, cooperative interactions between distinct subunits may establish structures, distributions and functions of these membrane proteins (Alberts *et al.*, 2002). Notably, cooperative assembly is also fundamental to the linear polymerization of actin filaments and microtubules, wherein the nucleation mechanism is similar to cooperative single pore oligomerization (Oosawa and Kasai, 1962; Alberts *et al.*, 2002).

In conclusion, the three cooperative stages (dimer–dimer interaction, single pore assembly and aggregation of pores) substantially enhance the efficiency of assembly of oligomeric pores. Here, the results present the first application of single molecule fluorescence microscopy to the observation of cooperative oligomeric pore assembly for a bacterial toxin on target cell membranes. The detection of heterogenous oligomeric populations, based on single and multi-FRET analysis, is applicable for the study of individual protein interactions in live cells using conjugates fused with fluorescent proteins including CFP, GFP and YFP. In general, single-molecule observations and statistical analysis of populations of intermediates will be useful in understanding how single molecules are brought together into macromolecular complexes in cells.

Materials and methods

Design and preparation of proteins

The residues for cysteine substitutions in LukF (S45) and HS (K222) were selected based on: (i) the LukF structure (Olson *et al.*, 1999); (ii) the related staphylococcal α-heptameric pore (Song *et al.*, 1996); and (iii) the amino acid sequence homology between LukF, HS and α-hemolysin (Gouaux *et al.*, 1997). We modelled the structure of γ-hemolysin pore in hexamers or heptamers by fitting six or seven units of LukF into the structure of α-heptameric pores. The distances between S45 and K222 were estimated to be ~2.2 and 3.0 nm in the hexamer (Figure 1A2, left) and ~3.0 nm in the heptamer (Figure 1A2, right). The glutathione *S*-transferase (GST) fusion *pGEX-4T-1* plasmids *GST–LukF-S45C* and *GST–HS-K222C*, were transformed into *Escherichia coli* DH5α for expression of GST–LukF-S45C and GST–HS-K222C, respectively. GST–LukF-S45C and GST–HS-K222C bound to glutathione agarose were labeled with a 10-fold excess of TMR-6-maleimide (Molecular Probes) and IC5-PE-maleimide (Dojindo) for 30 min at room temperture, and then washed free of unreacted dyes. LukF–TMR and HS–IC5 were finally eluted after incubation with 40 U of thrombin.

The degrees of labeling were determined by percent of fluorophore-labeled proteins (10 μg) on SDS–PAGE (12%), using NIH Image Scion 4.02. These agreed with measurements of the absorbance of TMR and IC5 at 546 and 650 nm, respectively. The labeled mutants electrophoresed (Figure 1B, lanes 3 and 6) more slowly than did the non-labeled (lanes 2 and 5). No bands of non-labeled proteins were observed in lanes 3 and 6, confirming that the labelling of both mutants was >95%. The specificity of the cysteine labeling was confirmed by negative controls of wild-type LukF and HS (lanes 1 and 4). The spectral FRET overlap between TMR emission and IC5 absorption is 4.6×10^{15} nm^{4}M^{-1}cm^{-1}. The extinction coefficient of IC5 (ε = 220 000 M^{-1}cm^{-1}) is slightly smaller than that of Cy5 (ε = 250 000 M^{-1}cm^{-1}) while the spectral profile of IC5 is similar, but shifted to a wavelength 8 nm shorter than that of Cy5. The Förster distance between TMR and IC5 was 5.4 nm.

To make mutants as negative controls for interactions observed by FRET signals, Ser33 of LukF and Thr29 of HS located at the side-by-side interaction surface (Olson *et al.*, 1999) were mutated to His and Asp, respectively. Such point mutations dramatically inhibit interaction of $LukF_{S33H}$ with HS_{T29D}, resulting in no oligomer or pore formation, and an absence of hemolytic activity, although the mutants could bind well to the membranes. These mutants were combined with single-cysteine mutations ($LukF_{S33H/S45C}$ and $HS_{T29D/K222C}$) to label the thiol groups with TMR ($LukF_{33}$–TMR) and IC5 (HS_{29}–IC5), respectively, and were tested in the same system with LukF–TMR and HS–IC5.

Hemolytic titration assay

Hemolytic assays of LukF–TMR and HS–IC5 in phosphate-containing saline buffer (PBS) at pH 7.4 were performed as described previously with the wild-type proteins (Kaneko *et al.*, 1997), except that 0.1% bovine serum albumin (BSA) was added to prevent the binding of proteins to the tubes, the incubation temperature was 25°C, and the concentration of HRBC was 6×10^{10} cells/l (1% cells/vol).

Ensemble membrane binding assay of each component

Sample preparation. LukF–TMR or HS–IC5 at concentrations ranging from 250 pM to 100 nM were incubated with either 6×10^8 or 6×10^{10} HBRC/l, in PBS containing 0.1% BSA at 25°C for: (i) 10 min to measure equilibrium binding constants; or (ii) for different periods of time (1–30 min) to measure binding rates. Unbound proteins in the supernatant (F_s, H_s) were obtained by centrifuging the cells at 2000 *g*, and measured using a spectrofluorometer. When both components were incubated with the cells for 15 min, F_s and H_s were measured in a similar way. The initial concentrations of LukF–TMR (F_o) and HS–IC5 (H_o) applied to cells were determined by performing parallel incubations in the absence of HBRC.

Spectrofluorometer set-up. LukF–TMR and HS–IC5 in PBS containing 0.1% BSA were measured in a spectrofluorometer (FP-750, Jasco) under excitation of 532 nm (green) and 635 nm (red), respectively. Cut-off filters at 560 nm and 650 nm (Omega) were inserted in front of the fluorescence detector to reduce the light scattering of green and red, respectively. Oxygen scavengers (Funatsu *et al.*, 1995) were used to reduce photobleaching. Experiments were performed in triplicate and the detectable resolution was ~10 pM fluorophores.

Single-molecule imaging of oligomerization

Sample preparation. To visualize LukF and HS monomers, ~20 pM of LukF–TMR or 400 pM of HS–IC5 were individually incubated with HRBC (6×10^{10}cells/l) for 5 min at 25°C. To visualize the dimerization of LukF and HS, we incubated the ghost cells with low protein concentrations (75 pM of LukF–TMR and 750 pM HS–IC5), and then detected monomers and dimers in the presence of soluble proteins at equilibrium. However, as the crowded monomers prevented the precise analysis of oligomers, this method was applied only in measuring the association constant of dimerization. In the other experiments, both components were incubated with HRBC at 25°C for 15 min to reach equilibrium (oligomerization efficiencies at 15 and 30 min were similar). As LukF bound to HRBC more strongly than did HS, the ratio between LukF–TMR and HS–IC5 was also set at 1:10 to lower the background of TMR signals interfering with the detection of FRET-IC5 spots. The cells were then washed with PBS once to remove unbound toxins, homogenized in 5 mM Tris buffer, resealed to generate ghost cells using PBS, and finally adhered on L-polylysine-coated glass chamber in PBS containing oxygen scavengers.

TIRF microscopy set-up and imaging. Samples were observed under a TIRF microscope (Figure 3A; Funatsu *et al.*, 1995; Ishii *et al.*, 1999). LukF–TMR was excited by a Nd:YAG laser (TIM-6222, Transverse) at 532 nm, and HS–IC5 was excited by a diode laser (F44-30M, Coherent) at 635 nm. In Figure 3C, to distinguish spots corresponding to dimers, trimers and tetramers, the two lasers were switched on and off in an anticorrelated fashion. Emission signals were collected using an objective (plan Apo ×60, N.A 1.4; Olympus), split by a dichroic mirror (610 nm DM; Ashahi), and passed through barrier filters (580DF30 for TMR; 670DF40 for IC5, Omega). The fluorescence images were captured by a SIT camera (C2400-08, Hamamatsu Photonics) with an image intensifier (VS4-1845, Video Scope). Images were, in some cases, integrated for eight frames in tracing the intensity of fluorescence (Figure 3B4, left), and in other cases for 32 frames in measuring the intensity of fluorescence to

improve the ratio of signal-to-noise. Thus, the spatial and temporal resolution of this system is 80 nm (pixel size) and 266 ms or 1.1 s, respectively. Adobe Photoshop was used for multi-color featured imaging: white spots showing signals for TMR, FRET-IC5 and IC5 were filled with green, orange and red, respectively. Offset was made with errors up to 10% in every image for easy detection of FRET spots from background. NIH Image with a custom macro program was used for analysis of photobleaching steps.

Data analysis. For the visualization of each component, mean intensity values of LukF–TMR (n = 97) and HS–IC5 (n = 106) molecules were 1.0 ± 0.39 and 1.0 ± 0.42 arbitrary units (a.u.), respectively. Those single spots emitted almost constant intensities with average life times of 10–30 s, then photobleached in one step, proving that membrane-bound LukF–TMR and HS–IC5 were monomers. The monomers exhibited two styles of motion on the membranes, restricted movements (D ≈ 1–5 × 10^{-2} μm²/s; 16 per total 29 spots for LukF–TMR, and 16 per total 27 spots for HS–IC5) and free bilateral diffusion (D ≈ 2–8 × 10^{-1} μm²/s; 13 spots for LukF–TMR and 11 spots for HS–IC5).

For FRET efficiency measurements of dimers (single-FRET of *F-H*), the 1 s-averaged images were used to analyze the TMR (I_{TMR}) and IC5 ($I_{FRET\ IC5}$) intensities on TMR excitation. Measuring the average intensities was appropriate in our case because random anticorrelated fluctuation between the donor and acceptor was not observed. The single-FRET efficiency was calculated as follows: FRET efficiency = $I_{FRET\text{-}IC5}/(I_{FRET\text{-}IC5} + \gamma I_{TMR})$ where γ is the correction factor which accounts for detection efficiency by the established microscope with the two dyes, determined to be 1.0 based on the method proposed by Deniz *et al.* (1999).

FRET-IC5 and IC5 intensities of spots representing trimers and tetramers were also measured from the 1 s-integrated images. Photobleaching steps of IC5 were analyzed from 30 ms interval images to critically confirm the reliability of the intensity deduction. In the assembly of larger oligomers, we estimated F_n-H_n based only on the FRET from multiple IC5 fluorophores in the oligomers (multi-FRET). The above equation for single-FRET efficiency was also applied to multi-FRET efficiency. Tracking the oligomers on the membranes, oligomers appeared to exhibit restricted motion, remaining essentially stationary, with D ≈ 1–3.5 × 10^{-2} μm²/s (dimers, trimers, tetramers), and there were a few freely-diffusing oligomers. The larger the oligomers/clusters were, the slower and more restricted their diffusion was observed to be.

Acknowledgements

We thank Y.Okada and L.Poole for critical reading of the manuscript. This work was supported by a grant-in-aid from the Ministry of Education, Culture, Sports, Science and Technology of Japan (H.H. and Y.K.). V.T.N. is the recipient of a scholarship from the Ministry.

References

Alberts,B., Alexander,J., Lewis,J., Raff,M., Roberts,K. and Walter,P. (2002) Protein. In Albert,B. (ed.), *Molecular Biology of the Cell*, 4th edn. Garland Science, New York, NY, pp. 147–162.

Alberts,B., Alexander,J., Lewis,J., Raff,M., Roberts,K. and Walter,P. (2002) The cytoskelton. In Albert,B. (ed.), *Molecular Biology of the Cell*, 4th edn. Garland Science, New York, NY, pp. 907–915.

Comai,M. *et al.* (2002) Protein engineering modulates the transport properties and ion selectivity of the pores formed by staphylococcal γ-hemolysins in lipid membranes. *Mol. Microbiol.*, **44**, 1251–1267.

Daugherty,M.A., Brenowitz,M. and Fried,M.G. (1999) The TATA-binding protein from *Saccharomyces cerevisiae* oligomerizes in solution at micromolar concentrations to form tetramers and octamers. *J. Mol. Biol.*, **285**, 1389–1399.

Deniz,A.A. *et al.* (1999) Single-pair fluorescence resonance energy transfer on freely diffusing molecules: observation of Forster distance dependence and subpopulations. *Proc. Natl Acad. Sci. USA*, **96**, 3670–3675.

Ferreras,M., Frank,H., Serra,M.D., Colin,D.A., Prevost,G. and Menestrina,G. (1998) The interaction of *Staphylococcus aureus* bi-component γ-hemolysins and leucocidins with cells and lipid membranes. *Biochim. Biophys. Acta*, **1414**, 108–126.

Funatsu,T., Harada,Y., Tokunaga,M., Saito,K. and Yanagida,T. (1995) Imaging of single fluorescent molecules and individual ATP turnovers by single myosin molecules in aqueous solution. *Nature*, **374**, 555–559.

Gouaux,E., Hobaugh,M.R. and Song,L. (1997) α-hemolysin, γ-hemolysin and leukocidin from *Staphylococcus aureus*: distant in sequence but similar in structure. *Protein Sci.*, **6**, 2631–2635.

Ha,T. (2001) Single-molecule fluorescence methods for the study of nucleic acids. *Curr. Opin. Struct. Biol.*, **11**, 287–292.

Ha,T., Enderle,T., Ogletree,D.F., Chemla,D.S., Selvin,P.R. and Weiss,S. (1996) Probing the interaction between two single molecules: fluorescence resonance energy transfer between a single donor and a single acceptor. *Proc. Natl Acad. Sci. USA*, **93**, 6264–6268.

Ishii,Y., Yoshida,T., Funastu,T., Wazawa,T. and Yanagida,T. (1999) Fluorescence resonance energy transfer between single fluorophores attached to a coiled-coil protein in aqueous solution. *Chem. Phys.*, **247**, 136–173.

Ishijima,A. *et al.* (1998) Simultaneous observation of individual ATPase and mechanical events by a single myosin molecule during interaction with actin. *Cell*, **23**, 161–171.

Kaneko,J., Ozawa,T., Tomita,T. and Kamio,Y. (1997) Sequential binding of Staphylococcal γ-hemolysin to human erythrocytes and complex formation of the hemolysin on the cell surface. *Biosci. Biotechnol. Biochem.*, **61**, 846–851.

Lakowicz,J.R. (1999) Time-resolved energy transfer and conformational distributions of biopolymers. In Lakowicz,J.R. (ed.), *Principles of Fluorescence Spectroscopy*. 2nd edn. Kluwer Academic/Plenum Publishers, NewYork, NY, pp. 395–424.

Mendelsohn,A.R. and Brent,R. (1999) Protein interaction methods: toward an endgame. *Science*, **284**, 1948–1950.

Miles,G., Movileanu,L. and Bayley,H. (2002) Subunit composition of a bicomponent toxin: Staphylococcal leukocidin forms an octameric transmembrane pore. *Protein Sci.*, **11**, 894–902.

Nguyen,T.V., Higuchi,H. and Kamio,Y. (2002) Controlling pore assembly of staphylococcal γ-hemolysin by low temperature and by disulfide bond formation in double-cysteine LukF mutants. *Mol. Microbiol.*, **45**, 1485–1498.

Okada,Y. and Hirokawa,N. (1999) A processive single-headed motor: kinesin superfamily protein KIF1A. *Science*, **283**, 1152–1157.

Olson,R., Nariya,H., Yokota,K., Kamio,Y. and Gouaux,E. (1999) Crystal structure of staphylococcal LukF delineates conformational changes accompanying formation of a transmembrane channel. *Nat. Struct. Biol.*, **6**, 134–140.

Oosawa,F. and Kasai,M. (1962) A theory of linear and helical aggregations of macromolecules. *J. Mol. Biol.*, **4**, 10–21.

Sako,Y., Minoghchi,S. and Yanagida,T. (2000) Single-molecule imaging of EGFR signalling on the surface of living cells. *Nat. Cell Biol.*, **2**, 168–172.

Schütz,G.T., Kada,G., Pastushenko,V.P. and Schindler,H. (2000) Properties of lipid microdomains in a muscle cell membrane visualized by single molecule microscopy. *EMBO J.*, **19**, 892–901.

Song,L., Hobaugh,M.R., Shustak,C., Cheyley,A., Bayley,H. and Gaoux,E. (1996) Structure of staphylococcal α-hemolysin, a heptameric transmembrane pore. *Science*, **274**, 1859–1866.

Sugawara,N., Tomita,T. and Kamio,Y. (1997) Assembly of *Staphylococcus aureus* γ-hemolysin into a pore-forming ring-shaped complex on the surface of human erythrocytes. *FEBS Lett.*, **410**, 333–337.

Sugawara-Tomita,N., Tomita,T. and Kamio,Y. (2002) Stochastic assembly of two-component staphylococcal γ-hemolysin into heteroheptameric transmembrane pores with alternate subunit arrangements in ratios of 3:4 and 4:3. *J. Bacteriol.*, **184**, 4747–4756.

Taguchi,H., Ueno,T., Tadakuma,H., Yoshida,M. and Funatsu,T. (2001) Single-molecule observation of protein-protein interactions in the chaperonin system. *Nat. Biotechnol.*, **19**, 861–865.

Tomita,T. and Kamio,Y. (1997) Molecular biology of the pore-forming cytolysins from *Staphylococcus aureus* α-hemolysin and γ-hemolysins and leukocidin. *Biosci. Biotechnol. Biochem.*, **61**, 565–572.

van der Goot,G. (ed.) (2001) *Pore-forming toxins*. Springer-Verlag, Berlin, Heidelberg, Germany.

Walluce,A.J. *et al.* (2000) *E. coli* hemolysin E (HlyE, ClyA, SheA): X-ray crystal structure of the toxin and observation of membrane pores by electron microscopy. *Cell*, **100**, 265–276.

Received May 19, 2003; revised August 8, 2003; accepted August 11, 2003